Skyrmionics—Computing and memory technologies based on topological excitations in magnets

(iD) **Hamed Vakili,** (iD) **Jun-Wen Xu,** (iD) **Wei Zhou, et al.**

View Online　　**Export Citation**　　**CrossMark**

ARTICLES YOU MAY BE INTERESTED IN

Skyrmionics—Computing and memory technologies based on topological excitations in magnets

View Online   Export Citation   CrossMark

Hamed Vakili,[1,a)] Jun-Wen Xu,[2] Wei Zhou,[1] Mohammad Nazmus Sakib,[3] Md Golam Morshed,[3]
Timothy Hartnett,[4] Yassine Quessab,[2] Kai Litzius,[5] Chung T. Ma,[1] Samiran Ganguly,[3] Mircea R. Stan,[3]
Prasanna V. Balachandran,[4] Geoffrey S. D. Beach,[5] S. Joseph Poon,[1] Andrew D. Kent,[2,a)] and Avik W. Ghosh[1,3,a)]

AFFILIATIONS

[1]Department of Physics, University of Virginia, Charlottesville, Virginia 22904, USA
[2]Center for Quantum Phenomena, Department of Physics, New York University, New York, New York 10003, USA
[3]Department of Electrical and Computer Engineering, University of Virginia, Charlottesville, Virginia 22904, USA
[4]Department of Materials Science and Engineering, University of Virginia, Charlottesville, Virginia 22904, USA
[5]Center for Materials Science and Engineering, Massachusetts Institute of Technology, Cambridge, Massachusetts 02139, USA

[a)]Authors to whom correspondence should be addressed: hv8rf@virginia.edu; sjp9x@virginia.edu; adk1@nyu.edu;
ag7rq@virginia.edu

ABSTRACT

Solitonic magnetic excitations such as domain walls and, specifically, skyrmionics enable the possibility of compact, high density, ultrafast, all-electronic, low-energy devices, which is the basis for the emerging area of skyrmionics. The topological winding of skyrmion spins affects their overall lifetime, energetics, and dynamical behavior. In this Perspective, we discuss skyrmionics in the context of the present-day solid-state memory landscape and show how their size, stability, and mobility can be controlled by material engineering, as well as how they can be nucleated and detected. Ferrimagnets near their compensation points are promising candidates for this application, leading to a detailed exploration of amorphous CoGd as well as the study of emergent materials such as Mn_4N and inverse Heusler alloys. Along with material properties, geometrical parameters such as film thickness, defect density, and notches can be used to tune skyrmion properties, such as their size and stability. Topology, however, can be a double-edged sword, especially for isolated metastable skyrmions, as it brings stability at the cost of additional damping and deflective Magnus forces compared to domain walls. Skyrmion deformation in response to forces also makes them intrinsically slower than domain walls. We explore potential analog applications of skyrmions, including temporal memory at low density—one skyrmion per racetrack—that capitalizes on their near ballistic current–velocity relation to map temporal data to spatial data and decorrelators for stochastic computing at a higher density that capitalizes on their interactions. We summarize the main challenges of achieving a skyrmionics technology, including maintaining positional stability with very high accuracy and electrical readout, especially for small ferrimagnetic skyrmions, deterministic nucleation, and annihilation and overall integration with digital circuits with the associated circuit overhead.

I. THE MEMORY LANDSCAPE

A. Introduction: The challenges of nonvolatile magnetic memory

Digital electronics has been driven for several decades by sustained hardware scaling and Moore's law. With the recent slowdown in Complementary Metal Oxide Semiconductor (CMOS) hardware and rapid growth of software, and with the migration from cloud computing toward edge devices, there is a strong impetus to re-examine the limits of computing. In the conventional Von Neumann computer architecture, the digital processor needs to access data stored in separate memory banks in order to perform logic operations. Unfortunately, the speed of memory scaling ($1.1\times$ in every 2 years) has not kept up with the drastically increased speed of processor scaling ($2\times$ in every 2 years). This increasing gap between memory and processor performance, the

so-called *memory wall problem,* is considered one of the main bottlenecks to increasing computer performance.

To mitigate the memory wall problem, a multi-level memory hierarchy is used, with the most frequently invoked instructions and datasets stored in a high-speed on-chip cache so that they can be accessed and executed efficiently by the processor. On-chip cache memory is typically built out of static random access memory (SRAM). However, SRAMs need at least six transistors per bit and are, therefore, expensive and limited in capacity, requiring significant off-chip access to dynamic random access memory (DRAM). Each DRAM cell involves a compact capacitor–transistor pair but is slow and energy hungry as it needs a regular refresh to replenish data that leaks from the capacitor, increasing the number of clock cycles for off-chip data access. A lot of active research is thus focused on developing a memory technology that can match the speed performance of SRAM and the high density of DRAM. Magnet-based nonvolatile memory is an emerging candidate addressing that technology bottleneck.

Magnetic memory has a rich history, with field-switched magnetic RAMs (MRAMs) and spin-transfer torque based RAMs (STT-RAMs) now being commercialized.[1–3] MRAMs are hard to scale because the scaling of the drive circuit requires increasing current densities with increasing energy dissipation. STT-RAMs have better-scaling properties, as switching is due to spin-polarized currents directly injected into a magnet across the oxide of a magnetic tunnel junction (MTJ). STT-RAM has evolved since the discovery of giant magnetoresistance in the late 1980s[4,5] and theoretical ideas soon after[6–8] to a dark horse in the 2000s[9,10] to becoming now a commercially viable candidate for on-chip cache memory.[11] With both the integration density of DRAM and comparable performance to SRAM,[12] STTRAMs benefit further from their compatibility with CMOS processes and voltages, zero standby leakage, scalability, high endurance, high retention time, and overall reliability. In particular, the density advantage compared to transistor-based volatile SRAM can be quite useful in designing a high-capacity non-volatile on-chip last level cache in the multi-level memory hierarchy, with a significant potential reduction in the number of off-chip DRAM access operations.

One of the significant challenges with the widespread adoption of STT-RAMs as a universal memory technology is the high write energy and low read speed of STT-RAM cache memory relative to CMOS on-chip cache. These shortcomings can be reduced by trading against the retention time, the energy barrier between binary states. Longer access times, along with the high error rates, pose other challenges in using STT-RAM for on-chip cache. In short, there is an overall energy-delay-error trade-off.[13] The error rate of STT-RAM can be mitigated by adopting intelligent array-level design techniques; however, they do not maximize STT-RAM benefits. The error rate problem gets exacerbated, and the robustness of STT-RAM suffers while it is scaled down, requiring stronger error correction schemes and a compromised energy efficiency benefit. Requirements like bidirectional write currents, asymmetry in the critical write currents, single-ended sensing operation, and shared current paths for read and write impose further challenges in establishing STT-RAMs as a replacement of last level cache.

Part of the energy hungriness of STT-RAMs arises from the writing of information, where current needs to go through a high resistance tunnel barrier needed to protect the two binary memory states along a shared read line. Structures with orthogonal read–write paths, such as those using spin–orbit torque (SOT-RAMs) provide a possible way out—a metallic path used to write information, separate from an orthogonal read path, which can again be via a magnetic tunnel junction.[12]

This brings us to the evaluation of bits encoded by topological (solitonic) excitations in thin magnetic films, such as line-like domain walls and circular skyrmions. Such excitations can encode information in ultrasmall volumes below the thermal superparamagnetic limit that constrains regular magnets. The solitons can be driven at high speeds by modest currents along magnetic racetracks with low energy dissipation in heavy-metal underlayers, generating unique device applications. The high density of ultrasmall skyrmions stabilized somewhat by their topological barriers, as well as their quasi-ballistic, tunable, and linear dynamics are particular attributes that make skyrmionic devices potentially useful in a variety of applications.

The purpose of this Perspective is to go over the factors controlling the size, dynamics, lifetime, and switching of isolated skyrmions, the material classes that support them, and their potential utilization for conventional or unconventional computing applications. The structure of this paper is as follows: In Sec. I, we go over the memory landscape. In Secs. II and III, we describe the fundamental physics based and material based limitations and parameter dependencies of skyrmions and domain walls, along with experimental characterization. In Sec. IV, we propose skyrmion based device applications. Finally, in Sec. V, we discuss the challenges and opportunities for a skyrmionic technology.

B. Energy-delay-error trade-off: Skyrmions as small, stable mobile magnets

One of the performance metrics of any binary switch is its energy-delay product, arguing for schemes that lower both their power dissipation and overall latency. The energy-delay product can be written as $I^2 R_{on} t^2 = Q^2 R_{on}$ with $t = Q/I$, where Q is the amount of charge needed to switch from off to on and R_{on} is the on-state resistance. The charge Q needed to switch a small magnet is set by (a) the minimum critical charge Q_c needed to switch magnetization, mandated by angular momentum conservation and (b) an added overdrive $Q/Q_c \gg 1$ required to reduce the dynamic write error rate (WER) or switching time to application-specific targets. This charge gets smaller for small volume magnetic excitations but so does the energy barrier that sets the thermal stability for data retention. Technologies such as Heat Assisted Magnetic Recording (HAMR) and bit patterned recording attempt to address this specific challenge. HAMR reduces the anisotropy barrier quickly through spot heating over a localized size and then allowing it to restore through fast cooling. Bit Patterned Recording breaks the magnet into tinier lithographically patterned ordered grains that can individually switch quickly but gain volume stability through strong inter-grain exchange interactions. A third way to get small stable magnetic excitations is by nucleating metastable skyrmions, essentially tiny mobile magnets, held together against thermal fluctuations by their topological properties.

We can study the temporal statistics of a small magnet using the Landau–Lifschitz–Gilbert–Slonczewski (LLGS)[7,10] equation

with a stochastic thermal torque or, equivalently, a Fokker–Planck equation for the probability distribution function of the magnetization.[13,14] For a small magnet with perpendicular magnetic anisotropy in an MTJ, we can get the time-dependent WER from an analytical solution to the 1D Fokker–Planck equation.[7,10,13,14] For large overdrive STT current $i = I/I_c \gg 1$, this works out to be[15]

$$\text{WER}_{\text{STT}}(t) \approx \frac{\pi^2 \Delta_{\text{th}}}{4} e^{-2Q/Q_c}, \quad Q = It, \quad (1)$$

where the critical current I_c is set in turn by a critical charge that satisfies angular momentum conservation between conduction electron and flipped magnetization,

$$\underbrace{\left(\frac{Q_c}{q}\right)}_{N=n\Omega} \frac{\hbar}{2} P\gamma = M_s \Omega (1 + \alpha^2), \quad (2)$$

where P is the spin polarization of the current, n is the electron density, q is the charge of an electron, $\gamma = g\mu_B/\hbar$ is the electron gyromagnetic ratio, $\hbar$ is the reduced Planck's constant, g is the electron dimensionless magnetic moment or g-factor, μ_B is the Bohr magneton, μ_0 is the permeability of free space, M_s is the saturation magnetization, α is Gilbert damping, Ω is the volume of the magnetic layer, and $\Delta_{\text{th}} = E_B/(k_B T)$ is the energy barrier, with $E_B = \mu_0 H_k M_s \Omega/2$ for magnetization reversal divided by the thermal energy and Boltzmann's constant k_B times the temperature T. The critical current density is given by[16,17]

$$j_c^{\text{STT}} = \frac{2q}{\hbar} \frac{\alpha}{P} \mu_0 M_s H_k t_{\text{F}}, \quad (3)$$

where t_{F} is the magnetic layer thickness and H_k is the anisotropy field. The interesting observation is that the critical switching time set by the ferromagnetic resonance frequency and the damping, $\tau_D = (1 + \alpha^2)/(\alpha\gamma\mu_0 H_k)$, increases as we reduce the damping. However, the critical current $I_c = Q_c/\tau_D = 2q\alpha E_B/(\hbar P)$ decreases such that Q_c is independent of anisotropy and weakly dependent on damping and is *set primarily by angular momentum conservation*.

The equations above set the charge Q required for writing information at a given speed and error rate. The demand for a low error rate, $\sim10^{-9}$ for memory and $\sim10^{-15}$ for logic, will require a significant overdrive $Q \gg Q_c$. In a 20 nm diameter magnetic layer of

2 nm thickness, CoFeB magnet of saturation magnetization $\mu_0 M_s \approx 1$ T with about 10^4 spins, assuming a Gilbert damping of $\alpha = 0.01$ and polarization $P = 0.7$, we get Q_c/q about 8×10^4 electrons for destabilization. Assuming an anisotropy energy ~350 kJ/m^3, we get an energy barrier $E_B \approx 30 k_B T$, which implies an overdrive with $Q/q \approx 10^6$ electrons at an error rate of 10^{-9}. At 1 ns switching time, the current density ≈50 MA/cm^2.

While the critical current is set by the magnet's energy barrier E_B and the charge by angular momentum conservation, the dissipated energy $E_{\text{diss}} = I^2 R_{\text{on}} t$ is several orders of magnitude higher. This is because the voltage needed to produce the necessary current is set by the resistance of the oxide tunnel barrier R_{on}, whose energy barrier is much larger than that of the switching magnet.

The energy dissipated can be reduced in all metallic devices such as proposed race track memories (Table I), where a spin current is injected into a metallic magnet from a heavy metal underlayer and the magnetization state read with a vertical current (e.g., a current passing through a tunnel barrier between the magnetic film and a fixed magnet with much higher anisotropy barrier), thus separating the read and write paths. Spin–orbit interactions in the heavy metal inject a spin perpendicular to the metal–magnet interface. The corresponding spin–orbit torque (SOT) can be used to flip a magnet. The current density can once again be obtained from energy considerations, while the write error rate obtained using a 2D Fokker–Planck equation with in and out-of-plane fields. Assuming small in-plane field H_x compared to the anisotropy field H_k, i.e., $h_x = H_x/H_k \ll 1$ and a magnetization perpendicular to the heavy metal–magnet interface, the equations once again simplify as[13,20,21]

$$\begin{aligned} E_B' &= E_B\left[(1 - h_x)^2 - 2h_s(\pi/2 - h_x - h_s)\right], \\ h_s &= c_J/H_K, \quad c_J = (\hbar/2q)(J\theta_{SH}/M_s t_F), \\ j_c^{SOT} &\approx \frac{2q}{\hbar} \frac{\mu_0 M_s t_F}{\theta_{SH}}\left(\frac{H_k}{2} - \frac{H_x}{\sqrt{2}}\right), \end{aligned} \quad (4)$$

where E_B' is the modified energy barrier for the SOT mechanism an c_J is the coefficient of the spin–orbit torque term. Plugging typical numbers ($P \approx 0.7$, $\theta_{SH} \approx 0.2$, $\alpha \approx 0.3$, the same film thickness), we find $j_C^{SOT}/j_C^{STT} \approx P/\theta_{SH}\alpha \approx 10$, larger primarily because the STT anti-damping current is proportional to Gilbert damping α ($\alpha \ll 1$), while the SOT in this example acts perpendicular to the damping torque like a field-induced torque. However, the switching time is correspondingly reduced, and once again, the energy-delay

TABLE I. Comparison of proposed domain wall-based racetrack memory (RTM)[18] with other memory technologies, including spin-transfer torque-based random access memory (STT-RAM), resistive random access memory (RRAM), phase-change memory (PCM), and magnetic random access memory (MRAM). DW-RTM has lower predicted energy consumption, leakage power, and size, but DWs are typically limited by pinning at the racetrack edges, where skyrmions are purported to have a distinct advantage.[19]

Technology	Write/erase times (ns)	Write energy	Read times (ns)	Read energy	Leakage power	Endurance	Non-volatility	Cell size (F^2)
RTM	3–250*	Low	3–250*	Low	Low	$\geq10^{16}$	Yes	≤2
RRAM	20	High	10–20	Low	Low	10^{11}	Yes	4–10
PCM	>30	High	5–20	Medium	Low	10^9	Yes	4–12
MRAM	10–20	High	3–20	Low	Low	10^{12}	Yes	10–60
STT-RAM	3–15	High	3–15	Low	Low	4×10^{12}	Yes	6–50

product depends primarily on the switching charge Q, set in essence by angular momentum conservation and acceptable error rates. A further energy reduction happens as current flows through the lower resistance of the metal underlayer, which can be more than an order of magnitude lower than that of the MTJ's tunnel barrier.

Note that the critical charge Q_c depends on the volume of the switching free layer magnet Ω. It is, therefore, useful to scale the magnet down to reduce the energy-delay product. However, the energy barrier E_B and the thermal stability factor Δ_{th} also decrease, as a result, making the magnet thermally unstable (this is called the *superparamagnetic limit*), a challenge which the aforementioned HAMR and bit patterned recordings approaches address head-on. Topological excitations such as skyrmions have added protection coming from their spin texture, which adds an extra barrier to their erasure, in other words, to continuously deform them to alternate textures with different topological numbers—for instance—uniformly oriented spins in their ferromagnetic background. A set of high density solitons like skyrmions, domain walls, and a slew of variants can, in principle, be used to encode memory in a racetrack geometry and has potential advantages compared to alternate memory technologies (Table I).

C. Skyrmions and topological stability

How does topology play a role in downscaling magnets? It helps us engineer defects inside the magnet that can withstand thermal fluctuations. One class of topological excitations in thin magnetic films are called skyrmions and can be viewed as circular spin domains with an inverted core relative to the surroundings (Fig. 1).[22–32] Unlike small magnets that tend to get their spins randomized by thermal fluctuations, a skyrmion is stabilized by spatial inversion symmetry breaking. Indeed, the topological stability of skyrmion has been directly demonstrated by Je *et al.*,[33] with longer lifetimes observed for magnetic skyrmions than trivial bubble structures. In B20 materials lacking inversion symmetry like FeGe or MnSi, D_{2d} materials like Mn_2PtSn with tetragonal unit cells, and amorphous ferrimagnets like CoGd on heavy metals like Pt, the broken symmetry generates a Dzyaloshinskii–Moriya interaction (DMI) of the form $E_{DMI} = \sum_{ij} \vec{D}_{ij} \cdot (\vec{S}_i \times \vec{S}_j)$ between lattice sites labeled by (i, j). The spins accordingly try to orient perpendicular to this symmetry-breaking DMI field, $d\vec{r}/dt = \vec{D}_\perp$, which generates a pattern of 2D spin excitations that can be classified using Poincaré diagrams (Appendix A).[34] The spin texture can be stereographically projected onto a sphere excluding one of its poles (a Bloch point) so that a continuous deformation in an infinite 2D plane cannot eliminate the skyrmion (Fig. 1).

We can quantify the winding of a skyrmion with a topological index N_{sk} that influences its 2D energy barriers (Appendix B) and creates a metastable local minimum in its energy landscape, specifically an exchange term proportional to N_{sk}^2/R that creates a well curvature and a DMI term proportional to $-N_{sk}D$ that creates a well dip (Fig. 2). This winding number is set by the integral of the phase picked up by the evolving spins across the skyrmion boundary and relates to the spatial variation of the magnetization unit vector $\mathbf{m}$ in the 2D (x, y) plane $N_{sk} = \frac{1}{4\pi} \int dx dy\, \mathbf{m} \cdot (\partial \mathbf{m}/\partial x \times \partial \mathbf{m}/\partial y)$. The magnetization vector $\hat{m}$ is characterized by 3D direction cosines (θ, Ψ), while their spatial locations are described in 2D polar coordinates (r, ϕ), the two

sets related by $\Psi = N_{sk}\phi + \psi$, with vorticity N_{sk} an integer and ψ being the domain angle or helicity. The integral N_{sk} then simplifies to $[m_z(r = \infty) - m_z(r = 0)] \times [\Psi(\phi = 2\pi) - \Psi(\phi = 0)] = pN_{sk}$, where $m_z(r) = \cos\theta(r)$ and $[m_z(r = \infty) - m_z(r = 0)]$ is the polarity $p = \pm 1$. The m_z difference relates to the radial evolution of magnetization tilt from core to surrounding (e.g., skyrmions vs merons), while the ψ difference is the overall winding. For simplicity, in this paper, we take the polarization $p = 1$. The parameters ψ and N_{sk} can be determined by minimizing the DMI energetics of the skyrmion, from the integrals worked out in Appendix B. Topological protection, however, is not absolute, especially for metastable, isolated skyrmions. A skyrmion can be intrinsically annihilated due to thermal fluctuations that shrink it till it reaches a Bloch point where the atomicity of the magnet can change the winding number to zero abruptly. A skyrmion can also annihilate its winding more gradually through the Bloch point when it approaches edges and non-magnetic defects where finite size effects imply that the texture of the confined/defect-adjacent skyrmion no longer maps onto the whole sphere.

D. Key parameters for a skyrmionic device

For a skyrmionic device to be competitive with the existing and emerging technologies, the size of the skyrmion needs to be small to enable dense memory and a logic circuit design. Furthermore, the device should have properties like low energy cost, high frequency, and overall material stability with temperature and external magnetic fields. We elaborate on the various needs as follows.

1. Size

In a magnetic material, the competition between the different energy terms can stabilize an isolated skyrmion. The phase space of the material parameters can be calculated numerically and analytically (Sec. II). Depending on the specific memory technology, sub-50 nm skyrmions need to be stable enough over seconds (e.g., cache memory) to years (e.g., hard drive) at room temperature. Larger skyrmions tend to diffuse more aggressively, while smaller skyrmions tend to last shorter, pin easier, and are harder to read electrically. We will show that the saturation magnetization M_s can set the skyrmion size through the magnitude of stray fields, while the film thickness controls a balance between lifetime and derivability with interfacial spin torques.

2. Speed and operation time

For a skyrmionic memory device, the rate of data processing is set by the speed at which skyrmions can travel along the racetrack. The speed of a skyrmion is a key factor for low power skyrmionic devices. In order to achieve a high speed for skyrmions, small M_s, low Gilbert damping, and topological damping are required [Sec. II B, Eq. (6)]. When a very large current is applied to skyrmions, it has been reported[35] that skyrmions can be distorted or even get annihilated, which puts an upper limit on skyrmion operating current. A speed between 100 and 700 m/s is probably a suitable target for the nearly linear, quasi-ballistic operation of skyrmion devices.
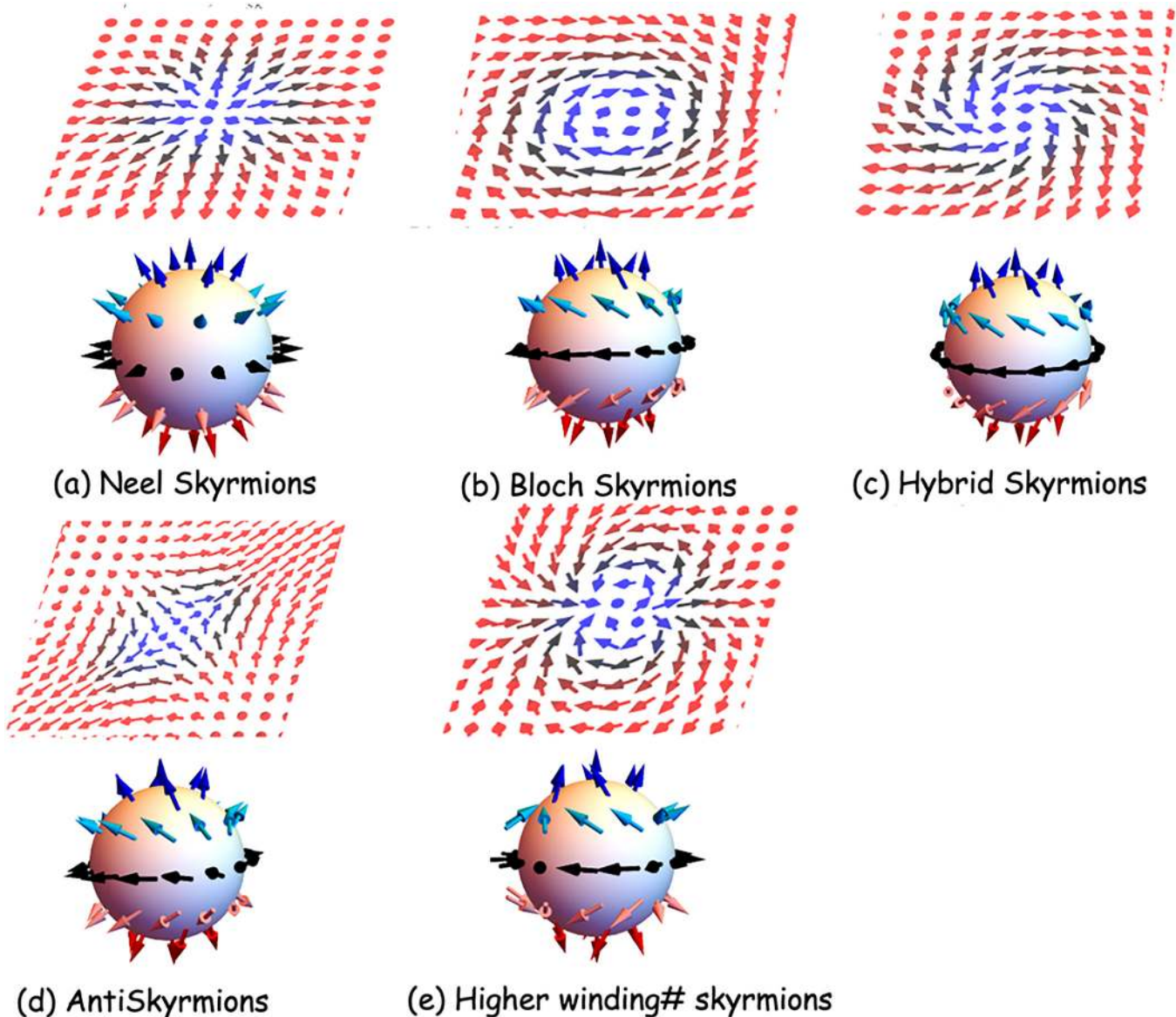
FIG. 1. 3D spherical arrangement of spins that generate 2D skyrmions through stereographic projection. The north pole becomes the skyrmion core while the south pole maps to the background spin texture. The figure shows skyrmions of various winding numbers N_{sk} with same polarization and various domain angles/helicities ψ. (a) Néel skyrmions (e.g., CoGd on Pt), $\psi = 0$, $N_{sk} = 1$. (b) Bloch skyrmions (B20 solids, e.g., FeGe), $\psi = \pi/2$, $N_{sk} = 1$. (c) Hybrid skyrmions (e.g., B20 on Pt), $\psi = \pi/4$, $N_{sk} = 1$. (d) Antiskyrmions (D2d tetragonal inverse Heuslers e.g., MnPtSn), $\psi = \pi/2$, $N_{sk} = -1$. (e) Higher winding number skyrmions (Frustrated FM, merging of two skyrmions with opposite vorticities), $\psi = 0$, $N_{sk} = 2$. These excitations map onto the usual classification of 2D linear excitations—stars for Néel skyrmions, cycles for Bloch skyrmions, spirals for hybrids, and saddle points for antiskyrmions.

3. Material stability

Due to the thermal dissipation from the applied electric current when a hypothetical skyrmionic device is operating, the temperature of the magnetic layer can increase well above the room temperature. In order to have a reliable operation, the magnetic layer needs to have a sufficiently high Curie temperature so that the

changes in temperature do not affect skyrmions too much. Additionally, if the device is expected to work under real-life conditions, it has to be resistant with respect to external magnetic fields.

A wide variety of materials have shown skyrmions so far. As we show in section, within this elaborate material set, *nearly compensated ferrimagnets and antiferromagnets with built-in PMA are*
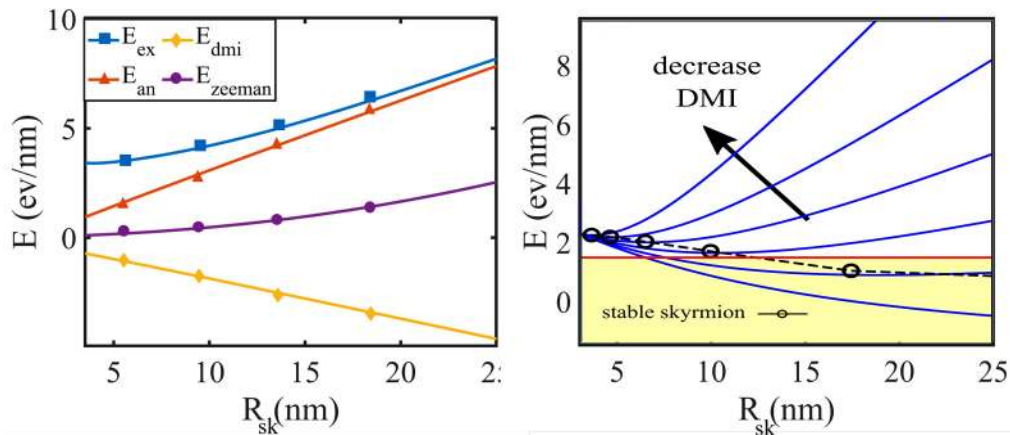
FIG. 2. (Left) Schematic of energy terms for a skyrmion. The 2D topological contribution to exchange $\propto N_{sk}^2 \Delta / R_{sk}$ and the negative DMI energy $\propto - N_{sk} \pi D$ together produce a local energy minimum for an isolated metastable skyrmion. (Right) Reducing DMI shifts the minimum to a lower radius, creating smaller isolated skyrmions while at the same reducing the energy well and thus their lifetime to dissolve into the background continuum. Increasing DMI increases skyrmion size, until at $D = D_c$ the skyrmion destabilizes into a stripe phase, indicated in yellow.

particularly important to skyrmionics. This is because the elimination of saturation magnetization enables a small lateral skyrmion size (and a correspondingly thicker film to restore stability that is hard with multi-layers), while also enabling low topological damping as well as a negligible contribution of external magnetic fields.

II. PHASE-SPACE FOR SKYRMIONS

Several parameters set the skyrmion static and dynamic properties—specifically saturation magnetization M_s, anisotropy field H_k, damping α, external magnetic field H_{ext}, DMI D and exchange stiffness A_{ex}. The phase space can guide us in choosing materials that, can host small skyrmions with long enough lifetimes. Additionally, a high Curie temperature, set primarily by exchange, is required to have the required material stability.

A. What determines skyrmion size?

A skyrmion has a circular core and a transition region (domain wall) to the background spin texture on the outside. By minimizing energy terms with respect to skyrmion radius and domain wall transition width, we get an equation for the skyrmion size. The skyrmion energy barrier then can be calculated from the skyrmion radius and width, as shown in Fig. 2. For a constant interfacial DMI, there is an optimized thickness that gives the maximum energy barrier. The points to note are that the energy barrier denoting skyrmion stability/lifetime is maximized for specific skyrmion radius and film thickness and that this barrier maximizing (and local energy minimizing) radius increases with DMI until a destabilization point where there is a phase transition to a skyrmion lattice. Lowering DMI for an isolated skyrmion lowers its size but also reduces thermal stability (Fig. 2) by making the metastable wells shallower and allowing the skyrmion to melt into the homogeneous magnetic background.

Minimizing the energy for an isolated skyrmion (Appendix B), we get the skyrmion size. The result at zero magnetic field is of the form[36–39]

$$R_{sk} = \left(\frac{D}{D_c} \right)^a \frac{C_1 \Delta}{\sqrt{1 - C_2 (D/D_c)^b}}, \quad \Delta = \frac{\pi D}{4K}, \quad (5)$$

where a, b, $C_{1,2}$ are size dependant fitting constants.[38,40] D is the DMI and A_{ex} is the exchange stiffness. The critical DMI is $D_c = 4\sqrt{A_{ex} K}/\pi$. Here, the effective anisotropy includes contributions from the demagnetization field and external fields $K \approx K_u - \mu_0 M_s^2/2 - \mu_0 M_s H_{ext}$. Equation (5) shows that a perpendicular magnetic anisotropy (PMA) K_u is required to stabilize a skyrmion in absence of a magnetic field. We also see that reducing saturation magnetization M_s increases the effective anisotropy through the elimination of stray demagentization fields. This reduces the lateral skyrmion size but also the depth of the energy well in Fig. 2 and thus the overall stability and lifetime. We can push up the lifetime (proportional to volume of skyrmion) by increasing the film thickness, which argues for nearly compensated ferri/antiferromagnets with built-in PMA as opposed to, say, multilayers.

B. What determines skyrmion speed?

To have a low latency skyrmion-based device, fast skyrmions at small energy costs are required. An efficient way to drive a skyrmion or a domain wall is using spin–orbit torque. A flowing charge current in a heavy metal underlayer creates a vertical separation of electron spins along the axis perpendicular to the metal–magnet interface. The accumulation of conduction electron spins at the interface creates an effective magnetic field causing precession of the skyrmion magnetic spins around it, leading to the movement of the skyrmion.[7,38,41–43] Using the rigid spin, Thiele approximation (Appendix C), we can write down the equation for the force on the

ith layer in a multi-sublattice magnet.[38] Solving for the corresponding magnetization dynamics, we can get the skyrmion velocity that once again arises from angular momentum conservation,

$$\boldsymbol{v}_{sk} = \frac{4\pi B \theta_{SH} R(\psi - \theta_0)}{\sqrt{\alpha^2 S(T)^2 \mathcal{D}_{xx}^2 + (4\pi S_N(T))^2}} \mathbf{j}_{hm}, \tag{6}$$

where $B = \pi \hbar I_0 / 2q$, $I_0 \approx \frac{1}{4}\pi R_{sk}[|N_{sk}| + e^{-\rho}/2\pi\rho]$, $\mathcal{D}_{xx} = \int dx dy$ $(\partial_x \hat{m} \cdot \partial_x \hat{m})$ is the dissipation tensor, $\rho = \frac{R_{sk}}{\Delta}$, and R is the 2D rotation matrix. $S(T) = \Sigma_i M_{s_i}(T) t_{F_i}/\gamma_i$ is the spin angular momentum summed over sublattices, $S_N(T) = \Sigma_i N_{sk_i} M_{s_i}(T) t_{F_i}/\gamma_i$ is the topological spin angular momentum, and $\tan \theta_0 = 4\pi \langle N_{sk} \rangle / \alpha \mathcal{D}_{xx}$, with the average topological index $\langle N_{sk} \rangle = S_N/S$. We see that even in the absence of dissipation, there is a topological damping term proportional to N_{sk} that limits the skyrmion speed compared to a domain wall. By reducing the saturation magnetization, as in compensated ferrimagnets or anti-ferromagnets, we see that skyrmions can reach considerably higher speeds than in ferromagnets. This is because fewer charges are needed to switch a vanishingly small magnetization so that for a given injected current, these fewer charges can drive the skyrmion along at much higher speeds. For speeds close to the magnon speeds v_m, relativistic effects have to be taken into account and the speeds become $v'_{sk} = v_{sk}\left[\frac{1+\sqrt{1-(v'_{sk}/v_m)^2}}{2}\right]$. At such limits, skyrmion will have an elliptical shape with $D_{x,y} = R_{sk}$ $(1 + [1 - (v_{sk}/v_m)^2]^{\pm 1/2})$, describing the minor and major axes, respectively (Appendix C).

The rotation matrix $R(\psi - \theta_0)$ tells us that there is a deviation from the current path due to a Magnus force, Θ_{SkH}, generating a skyrmion Hall effect

$$\frac{v_{sk,y}}{v_{sk,x}} \equiv \tan \Theta_{SkH} = \left(\frac{4\pi \langle N_{sk} \rangle \cos \psi - \alpha \mathcal{D}_{xx} \sin \psi}{4\pi \langle N_{sk} \rangle \sin \psi + \alpha \mathcal{D}_{xx} \cos \psi} \right). \tag{7}$$

The above equation suggests a constant skyrmion Hall angle independent of applied current density. However, a series of experiments[45,47,48] have recently shown that the skyrmion Hall angle in ferromagnets depends strongly on the applied drive. Several mechanisms have been proposed to explain this deviation from the Thiele model, such as pinning sites[44] that randomize the skyrmion trajectories in the creep and depinning regimes [see Fig. 3(a)]. Other proposed mechanisms that cause skyrmion deformations in the flow regime and contribute to a change in the skyrmion Hall angle[45,46] originate in a field-like spin–orbit torque contribution [Fig. 3(b)],[45] or in material inhomogeneities that induce random fluctuations in the skyrmion, which change the dynamics in a non-rigid way that is not included in the Thiele model [Fig. 3(c)].[46] Aside from the drive dependence of the skyrmion dynamics, no direct influence of thermal effects on the skyrmion Hall angle has been found (Fig. 4) over a wide range of temperatures. Let us now compare these skyrmion velocities with the simpler 1D DW

equations within the Thiele approximation

$$v_{DW} = \frac{\pi}{2} \frac{D_{int} j_{hm}}{\sqrt{(S_0(T) j_{hm})^2 + (\alpha S(T) j_0)^2}}. \tag{8}$$

With $S_0(T) = |S_1(T) - S_2(T)|$, $S = |S_1(T) + S_2(T)|$, and $j_0 = 2qt_F D_{int}/\hbar \theta_{SH} \Delta_0$. Once again for speeds close to the magnon speeds v_m, relativistic effects have to be taken into account. At such speeds a Lorentz contraction of the domain wall width happens, $\Delta'_0 = \Delta_0 \sqrt{1 - (v'_{DW}/v_m)^2}$,[49] whereupon the speeds become[50] $v'_{DW} = v_{DW}\sqrt{1 - (v'_{DW}/v_m)^2}$, where v_{DW} is the non-relativistic DW speed.

Note that Eq. (8) suggests that ferromagnetic domain wall speeds saturate to a constant $\propto D_{int}/M_{eff}$ for large current densities j_{hm} that sit in both the numerator and the denominator of the velocity term v_{DW}, leading to an overall damped motion (Fig. 5). This may imply that skyrmions could quickly overcome the speeds of a corresponding straight, 1D domain wall in the same material. However, it is important to realize that skyrmion speeds are furthermore dependent on internal spin dynamics, which start to dominate at high currents and are not captured by the Thiele equations. A simple example of this is the change in size and shape of a skyrmion, which occurs under the influence of a current.[45,46] In particular, at higher current drives, these effects can dominate the skyrmion dynamics, leading to an elongation of the skyrmion and the formation of a domain wall-like section within the otherwise round skyrmion. These, in turn, cause them to be driven by the same dynamics as domain walls. Together with other effects such as added topological damping, it becomes apparent that *a skyrmion cannot move faster than a domain wall under identical conditions.*

By applying a proper 1D domain wall model that accounts for the drive's pulse shape and inertial effects caused by domain wall spin canting (see Fig. 5), we find that skyrmions near the relativistic speed limit move at the same speeds as domain walls. This has been observed both in micromagnetic simulations as well as current-driven experiments on ferrimagnetic CoGd (Fig. 5). The relativistic speed limit increases strongly for antiferromagnets ($M_{eff} = 0$) with zero topological damping, while the limitation set by skyrmion distortion will still remain in place and prevent skyrmions from moving faster than domain walls. Even nanoscale skyrmions like those reported by Romming et al.,[51] with arguably the highest rigidity of all skyrmions (due to small size) being not impervious to the effect, as Fig. 5(d) shows. The mobility of the skyrmions (blue, orange, and green data) initially follows the linear mobility curve for undistorted skyrmions that can be derived from the Thiele equation.[38] However, after a critical current density is reached, the skyrmion cannot withstand the enormous torques any longer and collapses long before reaching the 1D domain wall limit (purple, red) in the material. The gray shaded area gives a phenomenologically determined stability regime for skyrmions, outside of which the skyrmion starts to loose its rigidity. Note that the slope of the Thiele mobility increases with decreasing magnetic field up to about 1 T, where it becomes too low to stabilize skyrmions in the material.
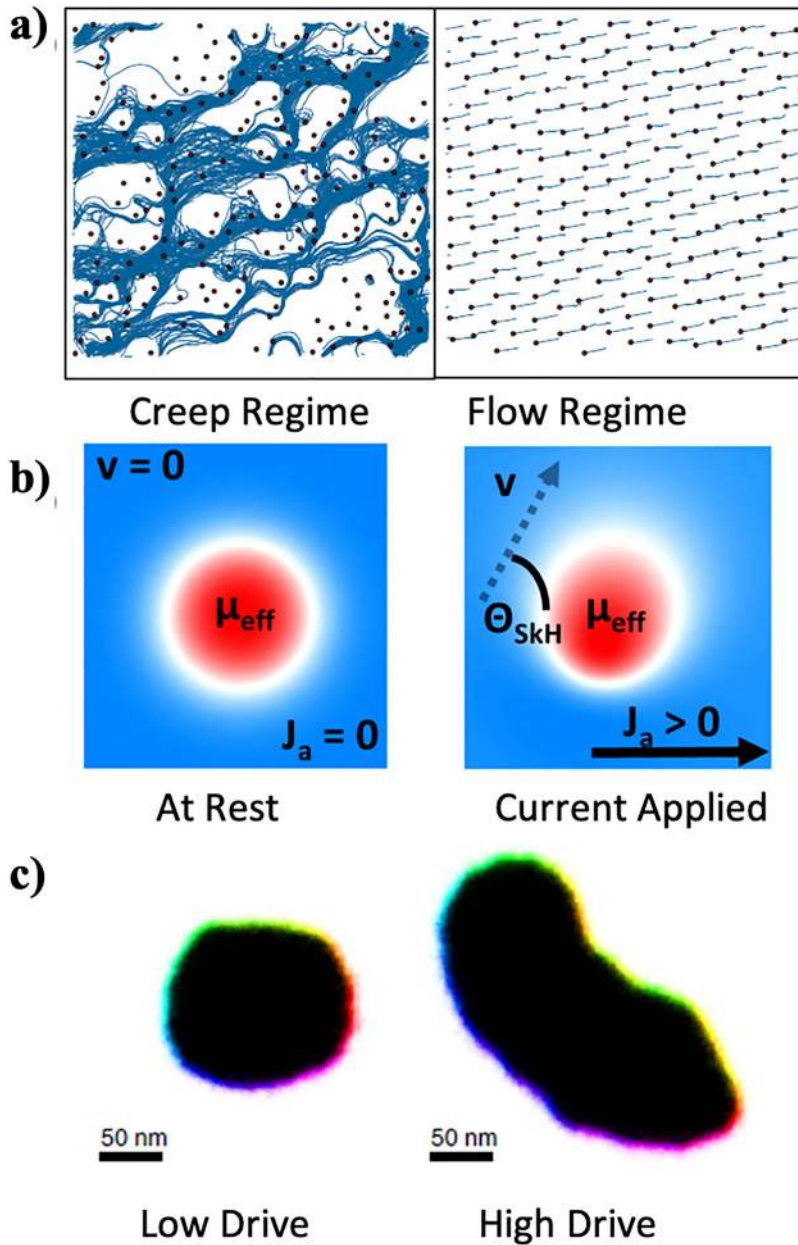
FIG. 3. Three mechanisms that change the skyrmion Hall angle. (a) Pinning sites in the material randomize the skyrmion trajectories at low current densities and thus reduce the skyrmion Hall angle. This effect is mostly present in the creep and depinning regime. Reichhardt and Olson Reichhardt, New J. Phys. **18**, 095005 (2016). Copyright 2016 Author(s), licensed under a Creative Commons Attribution (CC BY) license. (b) At high drives, skyrmions can be deformed by the field-like component of the spin–orbit torque, thus changing their effective size and the skyrmion Hall effect. Reproduced with permission from Litzius *et al.*, Nat. Phys. **13**, 170–175 (2017). Copyright 2017 Nature Publishing Group. (c) Additionally, bubble skyrmions can experience DW oscillations and size deformations that can alter the skyrmion Hall angle. Reproduced with permission from Litzius *et al.*, Nat. Electron. **3**, 30–36 (2020). Copyright 2020 Nature Publishing Group.

III. MATERIAL NEEDS FOR SKYRMION BASED DEVICES

A. Ferrimagnets for small, fast skyrmions

To get fast skyrmions, a crucial parameter is the Gilbert damping α [Eqs. (6), I C]. A number of half and inverse Heusler materials are predicted to have a very small α[52] due to the suppression of one of their spin channels (Table IV, supplementary material). In addition, they are predicted to be ferrimagnetic with high T_N.

Stable skyrmions at room temperature are necessary for skyrmion based devices. While room temperature skyrmions have been reported in ferromagnetic heterostructures, such as Pt/CoFe/MgO,[53] and multilayer stacks of Ir/Fe/Co/Pt,[54] their large stray fields, due to large M_S, limit how small these skyrmions can be. Alternatively, ferrimagnets, which has low M_S near compensation, have smaller stray field and thus can host smaller skyrmions[38] while pushing up their speed by decreasing the average topological index $\langle N_{sk} \rangle$ [Eq. (6)]. One of the most promising ferrimagnets is amorphous rare-earth-transition-metal (RE-TM), such as CoGd. Compare to multilayer stacks, which require thin magnetic layers (<2 nm) to maintain PMA, structural anisotropy in RE-TM[55]
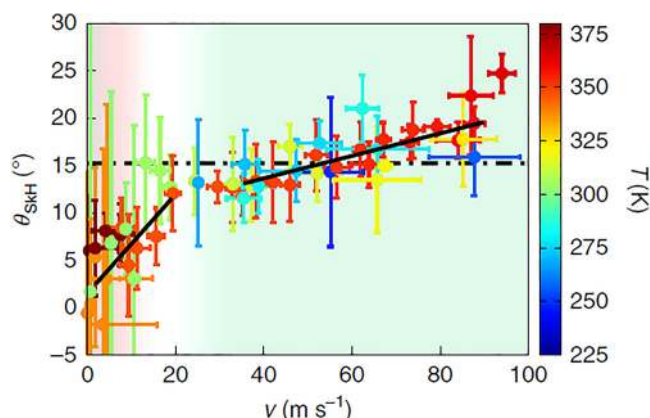
FIG. 4. Temperature and drive dependence of the skyrmion Hall angle. No significant temperature dependence of the skyrmion Hall effect was found when plotted against the skyrmion velocity. Note that the latter can experience temperature dependencies due to randomization of the torque and conductivity. Two regimes, corresponding to creep and depinning/flow regimes, respectively, are visible. Reproduced with permission from Litzius *et al.*, Nat. Electron. **3**, 30–36 (2020). Copyright 2020 Nature Publishing Group.

TABLE II. CoGd and Mn_4N are two promising ferrimagnetic materials due to their low M_s. Mn_4N has a very large Curie temperature that would make it stable at room temperature. Also shown are the DFT calculated M_s, K_u, and T_N parameters (calculated $J = 74.2$ meV) for the bulk ferrimagnetic Mn_4N using the experimental lattice constant value of 3.868 Å. Our 0 K DFT calculations predict an in-plane [100]-direction as the easy-axis magnetocrystalline anisotropy.

Material	M_s (kA/m)	K_u (kJ/m^3)	Size (nm)	T_N (K)
CoGd	100	50	10–150	450[56,58,69]
Mn_4N	87–100	88–100	100–300	745[70]
Bulk Mn_4N (DFT)	121.94	1376.11		740

allows the use of thicker (>5 nm) films to host skyrmions, which is crucial to enhance stability.[38] Furthermore, the low K_u of CoGd, in the order of 10^4 J/m^3 with relatively small interfacial DMI of 0.12 mJ m^{-2} in Pt/CoGd heterostructures,[56] fall within the parameter space of hosting ultrasmall (∼10 nm) and fast skyrmions (>100 m/s) at room temperature.

Simulations[57] and experiments[56,58] have reported skyrmions as small as 10 nm in RE-TM with heavy metal interfaces at room temperature. In atomistic simulations, sub-10 nm skyrmions are found to be stable at room temperature in 5–15 nm thick CoGd with a compensation temperature near 250 K. On the other hand, it should be noted that in experimental studies, the ultra-small skyrmions are much more difficult to image than larger, bubble-like skyrmions.
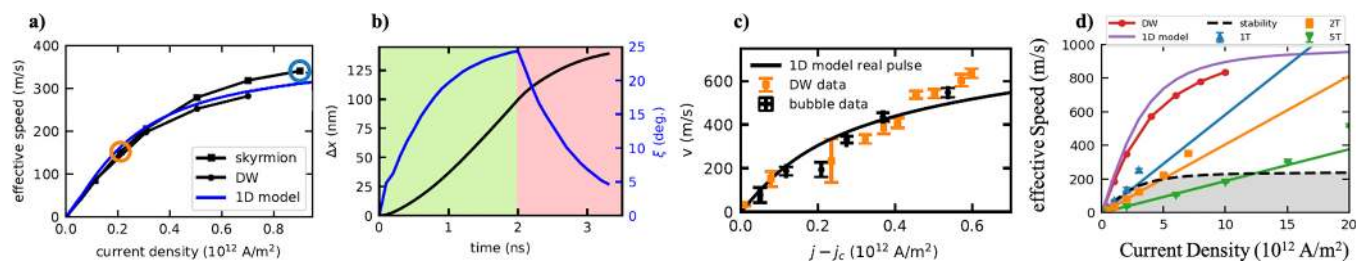
Only a few techniques are capable of imaging in the nanometer regime and simultaneously also recording time-resolved image sequences and applying stabilizing fields. The most prominent techniques currently are x-ray holography, scanning transmission x-ray microscopy (STXM), full-field transmission soft x-ray microscopy, and x-ray magnetic circular dichroism (XMCD-PEEM).[59,60] All these methods utilize the x-ray magnetic circular dichroism (XMCD) effect that leads to a magnetization-dependent absorption of photons in the material. An additional advantage of this technique is the element-specific resolution of recorded data, i.e., the absorption of only one atomic species can be selected to image sublattices and otherwise compensated materials such as ferrimagnets.

While CoGd is suitable for ultrasmall skyrmions at room temperature, a potential drawback for high-density storage application is thermal stability. An abrupt loss of PMA is reported in CoGd at 350 °C.[61] Such temperatures are often reached during complementary metal–oxide–semiconductor (CMOS) fabrication.[62] Since PMA is necessary to stabilize skyrmions in CoGd, poor stability of CoGd would delete any skyrmions during processing and render them useless for data storages. One potential material to overcome this challenge is anti-perovskite ferrimagnet Mn_4N, which also has small M_s and K_u in the order of 10^4 J/m^3.[63] More importantly, Mn_4N is synthesized at near 400 °C,[64] thus Mn_4 is compatible with CMOS processing (Table II). The DFT calculated values for M_s,

FIG. 5. Non-linearity of drive and deformation as the origin of skyrmion speed reduction. (a) Simulated skyrmion and DW speeds as a function of applied current density. In contrast to the Thiele model descriptions considering skyrmions as rigid particles (which expect the skyrmion motion to follow a linear trend), the speeds of DWs and skyrmions are, in fact, practically identical and follow the 1D DW model. (b) DW and skyrmion displacement (black line) increase even after the current is switched off due to inertial effects caused by the canting of spins in the wall (blue curve). This effect coupled with non-rectangular current pulses can prolong the displacement of skyrmions in an experiment. (c) Experimental observation of skyrmion and DW speeds and 1D model taking into account the pulse shape. No significant difference is visible. (d) Nanoscale skyrmions under stabilizing magnetic fields (1–5 T) compared with simulated DW speeds and DW 1D model. Instead of deformations, here the skyrmions are destroyed before they can overcome the DW speed limit. Taken from Ref. 35.
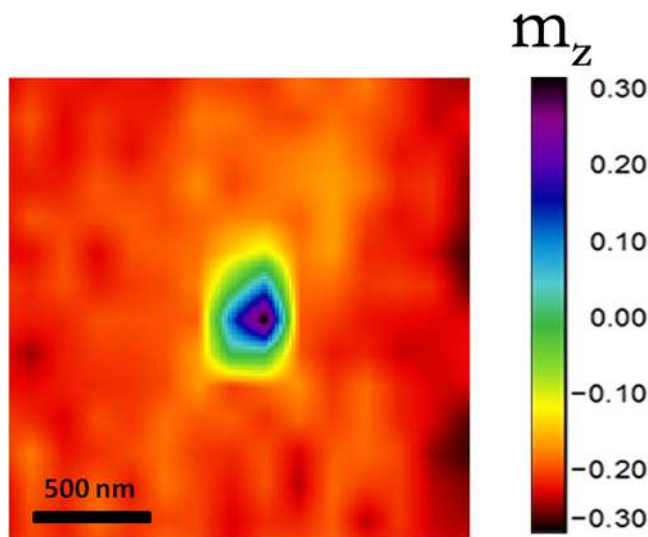
FIG. 6. Magnetic force microscopy (MFM) image reveals $\sim$300 nm skyrmion in Mn$_4$N (15 nm)/Pt on the MgO substrate. The red region corresponds to down magnetic moments; the dark blue region corresponds to up magnetic moments, which make up the core of the skyrmion.

K_u, and J in bulk Mn$_4$N using the experimental unit cell parameter value of 3.868 Å are also shown in Table II. The DFT parameters yielded a T_N of 740 K from our atomistic simulation, which is in excellent agreement with the experimental T_N of 745 K.[65–68] Figure 6 shows preliminary experiments of skyrmions in Mn$_4$N. Theory predicts the skyrmion size can be reduced significantly if we reduce the DMI from the underlayer, which we discuss next.

B. DMI engineering for skyrmion size and stability

To achieve ultrahigh density data storage and memory devices, we need to reduce the size of skyrmions and bump up their stability. As discussed in Sec. III A, we can do this with materials having a low saturation magnetization (to minimize the stray fields) plus a sizable DMI, such as in ferrimagnetic alloy thin films or multilayers[56,58,69] and synthetic antiferromagnets.[71,72]

The magnetization can be tuned by approaching the compensation temperature of ferrimagnets. How would we engineer the antisymmetric exchange or DMI parameter? At ferromagnet/heavy metal interfaces, the magnitude and sign of the DMI emerges from a complex interplay between (i) inversion symmetry breaking, (ii) interfacial contribution of the SOC of the HM metal (e.g., Pt/Co bilayers[73]), (iii) orbital hybridization between d states of HM layers (e.g., Au[74]) and magnetic layers as seen for Au underlayers, and (iv) transitions between the HM d orbitals near the K-points in the Brillouin zone, specifically, $d_{yz} \rightarrow d_{xy}$ and $d_{xz} \rightarrow d_{x^2-y^2}$.[75]

One way to tune the DMI is to influence the overall chirality with differential capping layers. For instance, a magnetic layer can be grown on a heavy metal like Pt/Co, and capped by one with weak DMI such as MgO[53,76] and TaO$_x$[56,77] or a strong negative DMI such

as Co/Ir. Using this additive method, an interfacial DMI $\sim$2 mJ/m^2 was reported in Ir/Co/Pt multilayers, allowing the nucleation of sub-100 nm skyrmions.[78,79] Similarly, one of the highest surface DMI constants $\sim$2 pJ/m was measured in an ultrathin Pt/Co (0.5 nm)/MgO stack, which was shown to host 130-nm skyrmions.[76]

An alternate way to control DMI is with a heavy metal alloy underlayer, providing a finely tuned inversion symmetry breaking mechanism at the interface.[58,80] By spatially grading the W composition x in a Pt/CoGd(5 nm)/Pt$_{1-x}$W$_x$ layer,[58] the interfacial DMI was tuned upto 0.23 mJ/m leading to the formation of sub-100 nm skyrmions. First principles calculations attributed this tuning and the subsequent saturation of DMI with increasing x to the continued reduction of SOC at the capping layer and simultaneous constancy of SOC at the underlayer [Fig. 7(a)].[81] Calculations also predicted DMI tuning with varying HM in Pt/CoGd/X (X = Ta, W, Ir), with W favoring the highest DMI while Ir producing a lower DMI. In another study, the interfacial DMI in Pd$_{1-x}$Pt$_x$/FeCoB/MgO showed a DMI increase by 5 as x is varied from 0 to 1.[80] Control of the spin-Hall efficiency was achieved as well, and a maximum spin-Hall angle of 0.60 was observed for Pd$_{0.25}$Pt$_{75}$, which could be of use for energy-efficient skyrmion dynamics induced spin–orbit torque.

Electric field control of the interfacial DMI has been recently demonstrated, with a 130% variation of DMI energy via voltage gating reported in Ta/FeCoB/TaO$_x$[82] [Fig. 7(d)].[82,83] By applying a negative voltage (-20 V), the authors were also able to shrink the size of stripe domains and skyrmion bubbles, as depicted in Figs. 7(b) and 7(c), respectively. It was observed that ionic gating modifies not only the DMI but also the anisotropy and the saturation magnetization.[83] Interestingly, ion (He$^+$) irradiation was also shown to lead to an increase in interfacial DMI and domain wall velocity in Ta/CoFeB/MgO due to disorder introduced at the interface.[84]

C. Controlled nucleation of isolated skyrmions

For technological applications, it is usually desirable to create, move, and annihilate skyrmions as a way of writing information. Therefore, materials where the skyrmion is a metastable state are more attractive, as opposed to ground state skyrmions,[85–87] and in this case, several methods can be employed to nucleate skyrmions, with proposed device applications.[88–90] One important requirement of any nucleation method is to be controllable as needed for the device it is being used for. To realize a reliable skyrmionic device, we need further investigation into the fundamental physics of nucleation and annihilation, and their potential control knobs.

1. Magnetic fields

A common nucleation method relies on the use of a magnetic field can be applied externally or locally (e.g., via an Oersted loop around a nanostructure[53]). In ferro- and ferri-magnetic films and multilayers with large demagnetization field, the ground state is formed by stripe domains that can be further shrunk into skyrmion bubbles.[48,53,69,71,72,91,92] Nevertheless, external magnetic fields are not compatible with the implementation of devices.
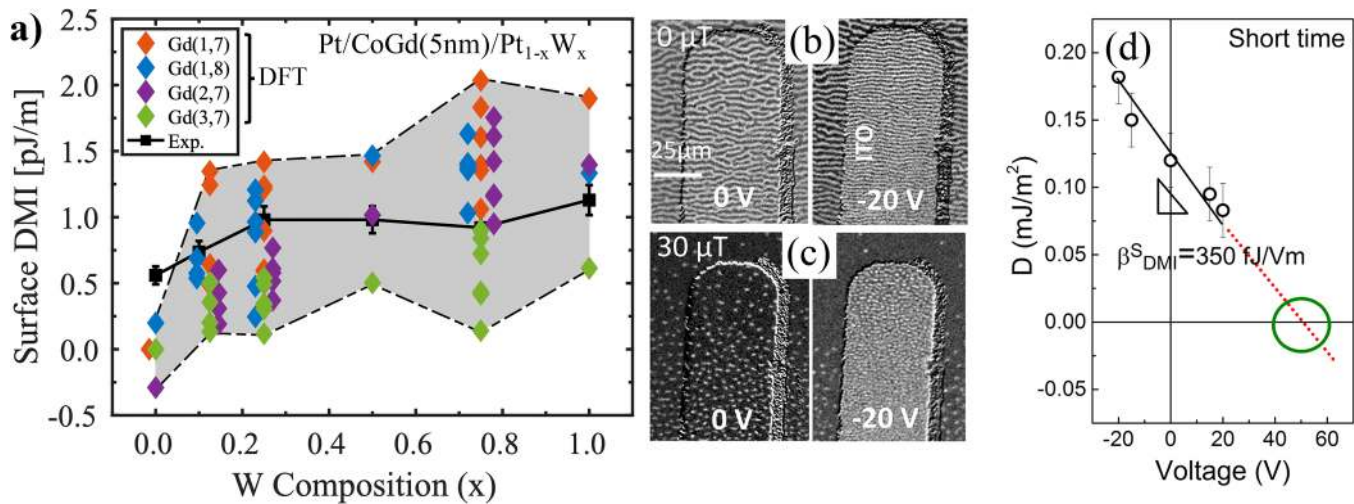
FIG. 7. DMI engineering (a) Evolution of the DMI energy as a function of the W composition in Pt/CoGd(5 nm)/Pt$_{1-x}$W$_x$ (modified from Refs. 58 and 81). Colored rhombuses are DFT calculations. (b) and (c) magneto-optical Kerr images of FeCoB/TaO$_x$ before and after applying a negative gate voltage at 0 and 30 μT, (d) variation of the DMI energy in FeCoB/TaO$_x$ as a function of the gate voltage. Reproduced with permission from Srivastava *et al.*, Nano Lett. **18**, 4871–4877 (2018). Copyright 2018 American Chemical Society.

2. Spin currents

On the other hand, several studies have reported the nucleation of metastable skyrmions by injecting an in-plane current in the presence of an out-of-plane magnetic field to provide stability.[56,79,91–93] Furthermore, some studies have reported that current pulses can be used to nucleate skyrmions without applying an external magnetic field.[91,94]

3. Joule heating

So far, the mechanism for the nucleation of metastable skyrmions has not yet been fully elucidated. Nevertheless, the use of current pulses, which are often applied over an extended period and with a large current density, suggests a nucleation mediated by thermal effects due to the Joule heating.[60,79,91] The nucleation of skyrmion arrays generally happens in the hottest area of the used wire devices and usually do not reliably nucleate single skyrmions. It is possible to produce similar results by application of millions of low current-density pulses that nucleates skyrmions on material inhomogeneities.[95]

4. Laser pulses

Alternatively, ultrafast nucleation of skyrmions using single ultrashort laser pulses was theoretically predicted[96,97] and demonstrated in a CoFeB thin film[98] and a ferrimagnetic TbFeCo alloy,[99] as well as TmIG.[100,101] Interestingly, no dependence on the light polarization was found; nucleation occurs even with linearly polarized light, which does not carry any angular momentum, thus demonstrating heating could be a sufficient stimulus to create skyrmions.[98]

5. Voltage pulses

Another method to nucleate or annihilate skyrmions is by using the Voltage Controlled Anisotropy (VCMA).[102–104] In this method, a skyrmion is nucleated or annihilated by applying electric field pulses. The applied electric field can change the perpendicular magnetic anisotropy (PMA). By lowering the anisotropy, the overall barrier for flipping of magnetic moments is also lowered, which would nucleate the skyrmion. Since the VCMA coefficient is not very large, the required voltage for skyrmion nucleation and annihilation is expected to be large ($\sim$7–20 V),[103,104] which would make its integration with an electric circuit challenging. This problem may be alleviated by building memory elements out of reshuttling skyrmions as in wavefront-based temporal memory, where occasional nucleation events can be used to replenish their finite lifetime at an energy cost that is readily amortized over multiple compute cycles. Alternatively, voltage control for magnetic exchange bias (EB) has also been proposed for skyrmion nucleation.[105–108] Electric field control of EB has been used to achieve a deterministic and reversible switching of the magnetization in the FM (FiM) layer which can be used for the precise creation of single skyrmions.[109] For the methods mentioned above, generally along a racetrack, the preferred locations of skyrmion nucleation would be at the defect sites, which already have lower anisotropy compared to their surrounding and thus a lowered barrier for nucleation. By using ion irradiation,[110] it is possible to engineer locations of the aforementioned defect sites in a controlled way, which, as we discuss in Sec. V, is critical for skyrmionic device reliability.

D. Skyrmion stability and lifetime

As reported earlier, a number of different methods[56,58,69] including STXM, MFM, and x-ray holography have imaged

10–150 nm skyrmions in CoGd. The time needed for these measurements suggests lifetimes of at least several hours. Since decade-long lifetimes are needed for many applications, computational estimates are crucial to providing guidance on skyrmion lifetimes.

To calculate skyrmion lifetimes, the transition-state theory (TST) for spin transition[111] has been employed. To use the TST, the minimum energy path needs to be calculated. Several studies have used the geodesic nudged elastic band (GNEB) method[112,113] to compute the minimum energy path for skyrmion annihilation. From the calculated minimum energy path, the attempt frequency f_0 and the energy barrier E_b are calculated and then the lifetime is extracted, $\tau = f_0^{-1} e^{E_b/kT}$. In the study by Wild et al.,[114] a variation of more than 30 orders of magnitude in the attempt frequency was reported, which could suggest a dominant role for the entropy effects compared to the energy barrier.

Recently, spin-polarized scanning tunneling microscopy has been used to locally probe skyrmion annihilation by individual hot electrons.[115] Such measurements can be quite useful for a better understanding of skyrmion lifetime under practical conditions. Room temperature lifetimes of up to 1 s were predicted for a 4 nm skyrmion in only a seven layer ferromagnetic film.[116] This result is very promising for long-lasting skyrmions at room temperature. According to the analytical model on skyrmions,[38] thicker films, and larger skyrmions increase the energy barrier to annihilate a skyrmion, which leads to longer lifetimes. This is especially encouraging for ferrimagnets, such as CoGd and Mn$_4$N. As discussed earlier in Sec. III A, intrinsic PMA allows the use of thicker films in these materials, so a lifetime of a decade may have already been achieved—and is certainly realistic. Our simulations with GNEB suggest that for 10 nm skyrmions, long lifetimes of up to 10 days are possible with CoGd thin films. For larger skyrmions >20 nm with thick films (>15 nm), year-long lifetimes seem feasible. Ultimately though, there is a trade-off between film thickness and drivability because spin–orbit torque acts near the magnet–heavy metal interface.

E. The role of defects and thermal diffusion

Defects in a racetrack play two crucial roles for skyrmion based devices. One, as mentioned, as a preferred location for deterministic skyrmion nucleation or annihilation. The second as a decisive factor in the dynamics and positional stability of skyrmions, which we now discuss.

Due to thermal effects, skyrmions in a race track can undergo diffusive displacement. If the racetrack is defect-free with little to no pinning sites, a skyrmion would be extremely susceptible to such thermal effects. This kind of random walk can be beneficial in stochastic applications of skyrmions, discussed later—but potentially destructive for some applications of skyrmions that encode analog information into their coordinates, as discussed in the context of wavefront memory in Sec. IV. Furthermore, skyrmions show inertia-driven drift shortly after a current pulse is removed, rather than stopping immediately [Fig. 5(b)]. One way to control such undesirable motion is by engineering confinement barriers such as point defects, or notches etched into the racetrack as missing material or with a different anisotropy. This would increase the periodic pinning of skyrmions uniformly along the racetrack,

instead of a random creep. But it should be noted the pinning must be small enough for the skyrmion to be movable by moderate magnitudes of current.

The mean squared displacement of a skyrmion due to diffusion can be described as[117,118] $\langle (r(t) - r(0))^2 \rangle = 4D_{\text{diff}} t$, where $r(t)$ is skyrmion position after time t, D_{diff} is the diffusion constant

$$D_{\text{diff}} = k_B T \frac{\alpha \mathcal{D}_{xx}}{(4\pi \langle N_{sk} \rangle)^2 + (\alpha \mathcal{D}_{xx})^2}. \quad (9)$$

By placing a notch (Fig. 8), it is possible to constrain a skyrmion's position. The skyrmion's positional lifetime to go from one side of a barrier to the other can be calculated from transition state theory, $\tau_p = f_0^{-1} e^{E_b/k_B T}$, where f_0 is the attempt frequency. Approximately an E_b of 30 $k_B T$ will result in positional lifetime of seconds for an attempt frequency f_0 of 10^{10} Hz.[120–122] In presence of a notch, the skyrmion needs to shrink in size in order to go past it, making it energetically unfavorable. The geometry and composition of the defect should be optimal so the skyrmion can be localized in equilibrium and driven past it with a modest drive current without being annihilated at the notch or the racetrack edge.

As seen in Fig. 8, the skyrmion positional lifetime can be long enough (years) for long-term memory applications and at the same have a moderate unpinning current. In Fig. 8, the material parameters are $M_s = 100$ kA/m, $A_{ex} = 12$ pJ/m, $K_u = 50$ kJ/m^3, 200 nm racetrack width, 5 nm thickness, and 100 nm notch radius. The notch is created by removing relevant parts of the racetrack in our
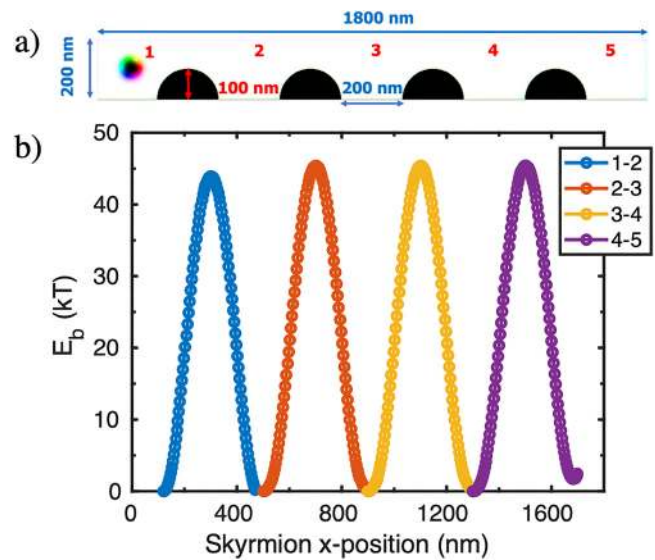

FIG. 8. (a) The racetrack geometry with four identical semicircular notches (radius 100 nm) separated by 200 nm from each other. The space between notches would be the places where the skyrmions would be positioned. (b) Calculated minimum energy path for skyrmion passing a defect using the parameters mentioned in the main text. By using the string method,[121] the MEP from one side of the defect to the other side is calculated. The minimum unpinning current is calculated to be a 4 ns current pulse of 1.4×10^{11} A/m^2.

model. By using a few of these notches consecutively, we find that it is possible to localize the skyrmion, in effect discretizing the skyrmion position.

IV. SKYRMIONIC DEVICE APPLICATIONS

The original racetrack idea[18] relied on a sequence of domain walls separating regions of opposite polarization, encoding the 0 and 1 bits. These domain walls on racetracks can have very high density, and the racetracks, in principle, can be stacked in 3D. However, domain wall motion is restricted by pinning and creep, especially near the edges. For skyrmions, information is contained in their absence or presence, but it relies once again on the ability of individual skyrmions to execute the particulate, quasi-ballistic, deterministic driven motion. While conventional densely sequenced DW/skyrmions-based memory is a possible application, there are other novel applications that can leverage the size and mobility advantages of such topological magnetic textures. We now discuss some of the device concepts involving skyrmions, including key operations needed such as read, write, erase and move. These applications could be key to building native memories and accelerators for applications such as temporal logic that leverages temporally encoded data for processing, stream-based computing that uses continuously streaming bits and is particularly oriented toward signal processing for building spiking neural networks, ultra-compact reservoir computing, and nano-oscillators. While all of these can be built using conventional CMOS technology, skyrmions may provide scalability due to the compactness of the circuits and low power consumption due to the physics of the skyrmion motion mapping onto the application model.

A. Magnetic memory for temporal computing

A recently proposed temporal computing scheme called race logic[124–126] has the potential to accelerate dynamic programming and machine learning algorithms. Information representation in race logic is different from the conventional Boolean approach as it represents multi-bit information at the arrival times of the digital rising edge of a single wavefront in a wire.[124] Such a unary temporal coding scheme potentially achieves orders of magnitude energy efficiency[124] compared to traditional binary data encoding, while accelerating dynamic programming algorithms can break a large optimization problem into smaller sub-problems. However, in Boolean computing, the analog temporal data needs to be converted to the digital domain, requiring a significant area and energy penalty from analog-to-digital converter circuits, limiting the computational capability. Thus, there is a need for a native analog temporal memory to store and retrieve the analog temporal data to enable complicated processing with the temporal coding scheme (Fig. 9).

Assuming a quasi-ballistic motion of skyrmion with an applied drive current, the time duration of a drive current determines the distance traveled by the skyrmion on the racetrack. Therefore, we can design a scheme of storing the temporal data in the position of a single skyrmion along the racetrack. This temporal data can represent timing delays in race logic for pattern matching applications, as well as thresholds for regular or automata decision trees for parallel processing of near-sensor serial input data.[126,127]
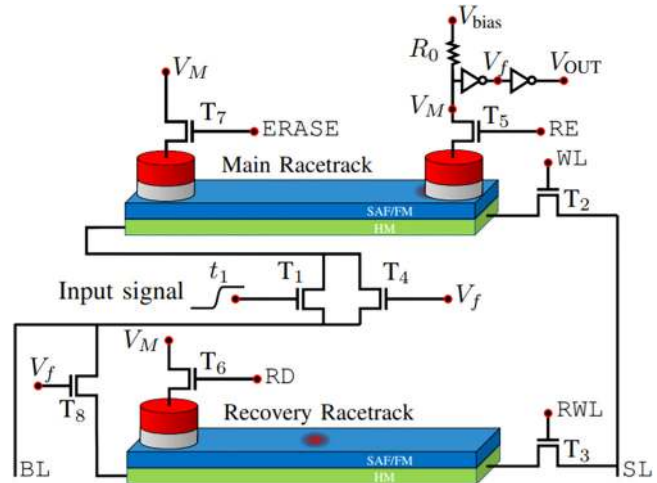

FIG. 9. Temporal memory circuit illustration and concept. The control lines consist of source line (SL), the bit line (BL), write line (WL), recovery write line (RWL), read enable(RE), recovery line (RD), and erase line (ERASE).[123] Note that only a single skyrmion per racetrack is used, with multi-bit information stored in the position of the skyrmion. Having a single skyrmion per racetrack increases its reliability and control over a packed, interacting array of skyrmions. Vakili *et al.*, *IEEE J. Exploratory Solid-State Comput. Devices Circuits* **6**(2), 107–115 (2020). Copyright 2020 Author(s), licensed under a Creative Commons Attribution (CC BY) license.

However, an adequate lifetime of skyrmions (Table III) will be needed to save on nucleation energy, as pre-written skyrmions can be reused rather than nucleating and destroying them repeatedly. Such a scheme allows for occasional replenishment of skyrmions through added voltage-gated nucleation events, whose cost is readily amortized over several (ranging from hundreds to millions) operating cycles.

Figure 10 shows the breakdown of energy dissipated in a typical skyrmion memory circuit (Fig. 9), resolved into individual components such as the eight transistors $T_1, \ldots, T_8$, reference resistance R_0 needed to generate voltage swings for reading, or the buffer used in the read circuitry, i.e., the inverter resistance. Notably, doing the full operation with CMOS memory instead of its skyrmionic counterpart would consume well over a hundred transistors to account for counters, storage latches, and decoders, at considerably larger energy cost and overall footprint. Furthermore,

TABLE III. Table of diffusion constants and corresponding ±40 nm skyrmion localization times at 1×10^{-8} inaccuracy.

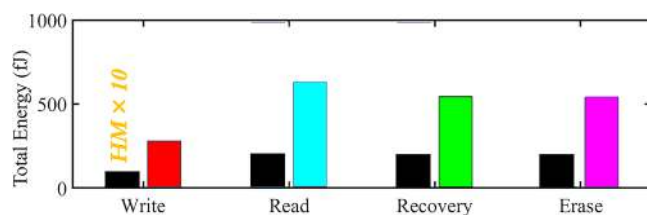| D_{diff} ($\mu m^2/s$)	Localization time (t)
1×10^{-2}[118]	Volatile (ms)
1×10^{-8}(CoGd)[119]	10^3 (s) (Cache)
1×10^{-10}	1 day
1×10^{-12}	1 year
42 k_BT Barrier	10 years (hard drive)

FIG. 10. Energy breakdown racetracks (HM) energy consumption, multiplied by 10 to be visible, and total energy for 50% duty cycle. A set of 640 nm racetracks used to capture wavefront and provide the energy breakdown. The high over-drive voltage of transistors consume the largest energy in all operations. Both the racetracks and the associated transistors are active during the read and recovery operation, resulting in consuming most energy. However, joule heating in the main and recovery racetracks contributes only a small fraction of the overall energy.[123]

the skyrmionic circuit has increased efficiency due to our ability to playback the wavefront duty cycle at low damping, making the energy-delay product another $32\times$ lower per cycle than 1 GHz CMOS. If we do 10–100 reads per cycle, the product is almost $2500\times$ lower. Finally, there is energy saving from repeated read operations due to the non-volatility of the skyrmions.

B. Reconfigurable skyrmionic logic

A reconfigurable hardware fabric offers increased performance per Watt at a lower non-recurring design and fabrication cost than the Application Specific Integrated Circuits (ASICs). Field-Programmable Gate Arrays (FPGAs) are medium to large integrated circuits that can be programmed to repeatedly perform any desired digital logic without any extra engineering cost. A matrix of programmable logic blocks is interconnected by a routing fabric which is also programmable.[128] Static Random Access Memory (SRAM) Cells store the logic function data configurations in modern FPGAs. Moreover, SRAM cells also store the select bits from the multiplexers (MUXs). Though FPGAs' re-programmability and manufacturing simplicity are advantageous, the use of high cost per bit and volatile SRAM cells leads to large area overhead. In this context, reconfigurable logic using skyrmionic racetracks carries the potential to bring non-volatility to FPGAs, thus obliterating the security concerns of programming the FPGA only at power ON. Moreover, reconfigurable logic using skyrmionic racetracks can be a promising alternative to the high-cost SRAM cells in FPGAs, as they can be much more densely packed than the SRAM-based designs which exhibit reasonable propagation delay.

Skyrmions and domain walls need spin current for their operations and can be used for ultra-small, low power, and nonvolatile memory or logic operations. Both skyrmions and DWs can have reasonably long lifetimes and high speeds. Skyrmions tend to have lower pinning than DWs, so the energy requirements can be lower. Nevertheless, one major difference between DW and skyrmion is that the DW can only move in the direction of the racetrack (1D movement). In contrast, the skyrmion can move along both axes of the racetrack (2D movement) due to their Magnus force. By exploiting this extra degree of freedom and the self converging nature of

skyrmion discussed shortly, a reconfigurable logic device can be designed with only one nucleation site. In Ref. 129 by using the merging, duplication, and skyrmion's ability to deform to a double domain wall and back, a logic device has been proposed, which demonstrates some of the interesting dynamical behavior of skyrmions.

Skyrmion-based reconfigurable logic has been proposed in Refs. 130 and 131. However, the device[130,131] needs extra fine-tuning of the parameters to get the reconfigurability. By leveraging the interaction between the skyrmions combined with the electric-field-controlled magnetic anisotropy (VCMA) effect, a reconfigurable logic gate is proposed in Ref. 131. However, both the reconfigurable logic gates[130,131] need at least two nucleation sites and more than one energy-hungry skyrmion nucleation event to do logic computation. An alternate reconfigurable device concept using self-focusing of skyrmions is proposed in Refs. 132 and 133, eliminating the need for fine tuning or the presence of skyrmion-skyrmion repulsion and requiring instead just a single skyrmion.

A skyrmionic AND–OR gate is proposed by using two joint racetracks with a notch [Fig. 11(a)] under the assistance of voltage control magnetic anisotropy (VCMA).[134] By accurately controlling the gate voltage V_{g1}, V_{g2} and the current density j_{SOT} with time [Figs. 11(b) and 11(c)], the motion of the skyrmions can be guided along the racetracks. Ultimately, such schemes need to be evaluated for their area-energy-latency costs and their overall accuracy, as some of the underlying operations need synchronization, such as with notches, to eliminate the deleterious effects of thermal diffusion.

C. Skyrmion gas based decorrelators for stochastic computing

Stochastic computing utilizes the statistical nature of noisy signals to achieve a collective result from an ensemble of readings. Unlike a Turing machine which uses deterministic devices to generate a deterministic output, stochastic computing uses probabilistic devices but generates a reliable output using systems-level techniques.[135] Compared with deterministic devices, stochastic devices consume much less energy while maintaining acceptable reliability of computation. Several complex circuit operations have been proposed, such as square rooting,[136] polynomial arithmetic,[137–139] and matrix operations,[140] as well as the "tan-sig" transform function employed in neural networks.[141–143] Similar simplified operations (sum + thresholding) arises from an OR gate.[144]

Essential to stochastic computing is the requirement that its input bitstreams are decorrelated. For example, in Fig. 12(a), we can see how the two binary strings fed into a summator generate a multiplication. String A encodes the number $P_A = \frac{6}{8}$ as the probability of getting a 1 (recorded by its time average), while string B encodes probability $P_B = \frac{4}{8}$. When passing through the summator (AND gate), the outcome probability of "1" is $\frac{3}{8}$, which is also the result of multiplication $P_A \cdot P_B$. However, this requires the two input strings to be decorrelated. We see that if the two input strings are perfectly correlated as in Fig. 12(b), the final output encodes P_A rather than P_A^2. Specialized decorrelator circuits can be constructed that sample a bitstream and generate an uncorrelated bitstream with the same mean value.

Broadly speaking, decorrelators can be categorized into three classes depending on their operating principle: (a) Regenerative
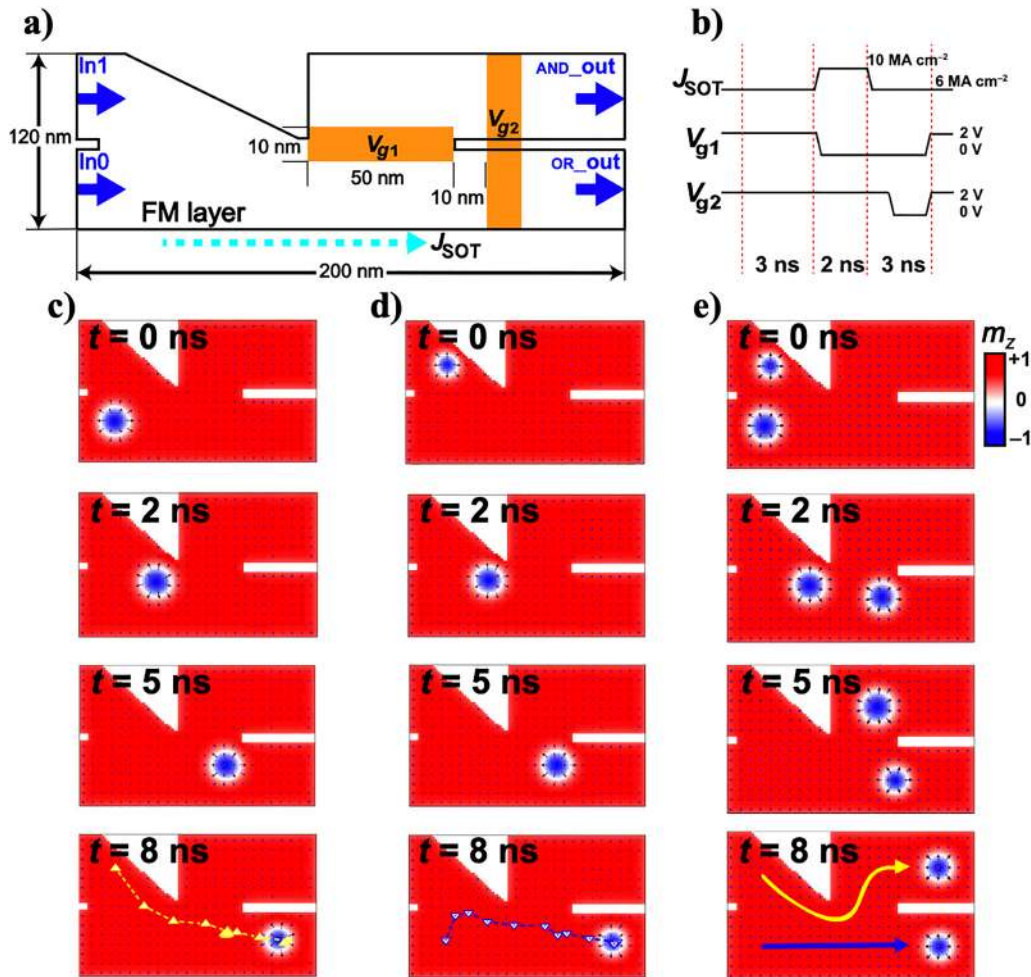
FIG. 11. Skyrmionic AND–OR logic device. (a) Device structure with two input lanes and two output lanes. The two electrode gates (with voltages V_{g1} and V_{g2}) are designed to modulate skyrmion motion through the VCMA effect. (b) Profile of driving current density (j_{SOT}) and positive voltages applied to achieve device function. (c)–(e) Three cases of inputs and their corresponding simulated processes and outputs. In the snapshots of the micromagnetic simulations, the color red represents spin up ($m_z = +1$), blue represents spin down ($m_z = -1$), and white represents spins that are horizontal in the plane ($m_z = 0$). Skyrmion trajectories are indicated in the magnetization snapshots at $t = 8$ ns. Reprinted with permission from Zhang et al., Phys. Rev. Appl. **13**, 054049 (2020). Copyright 2020 American Physical Society.[134]

decorrelator, which samples the input bitstream to first obtain a mean value and then generates a new output stochastic bitstream. This kind of decorrelator generates the best quality decorrelation but can stall computation due to the delay introduced in sampling. (b) Delay decorrelator that assumes a certain autocorrelation time of the bitstream source. The input bitstream is copied and "delayed" by a duration more than the autocorrelation time as the output bitstream. This ensures that the input and output bitstreams are uncorrelated due to the nature of the source signal. This is the preferred approach in pure CMOS-based decorrelators since we merely need to use a delay path (say, a shift register); however, a good quality decorrelator requires a priori knowledge of the bitstream source's autocorrelation time. (c) Reshuffling decorrelator [Fig. 12(c)] that first captures the input bitstream and shuffles their

order to generate the output stream, much like a deck of cards being shuffled after each game to ensure subsequent fair games. The quality of such a decorrelator depends on the length of the bitstream that can be recorded.

It has been proposed that a magnetic chamber, as shown in Fig. 13 can play an efficient role as a skyrmion-based reshuffling decorrelator. This device is demonstrated by modeling the ensemble dynamics in a collective coordinate approach where skyrmion-skyrmion and skyrmion-boundary interactions are accounted for phenomenologically. The skyrmions' order gets thermally reshuffled due to the diffusive 2D dynamical nature of interacting skyrmions at finite temperature. The output stream decorrelates from the input while maintaining the same probability. The predicted decorrelator is compact, at a footprint of μm^2, power of μW,
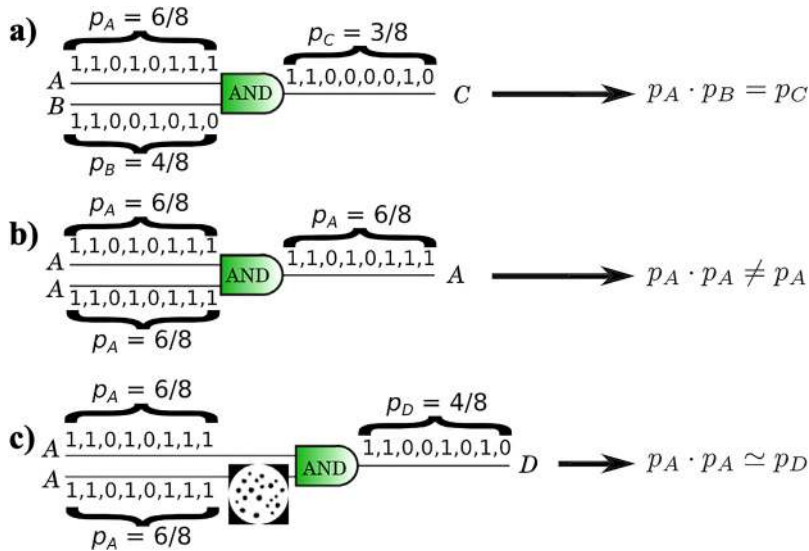
FIG. 12. (a) AND-gate implementation of the multiplication operation under the stochastic computing paradigm. The p-value of the output signal is equal to the product of the input signals' p values. (b) Whenever correlations exist between the input signals, the AND gate does not perform the expected multiplication. (c) Forcing the input signals through a skyrmionic reshuffler allows for a correct multiplication operation even in the presence of strong correlations between the input signals. Reprinted with permission from Pinna *et al.*, Phys. Rev. Appl. **9**, 064018 (2018). Copyright 2018 American Physical Society.[142]

and energy cost of ∼5 fJ/bit at 5 GHz. However, to keep the correlation small, the drive current and ultimately operational frequency need to be limited. Theoretical analysis shows a[142] 5% correlation for 200 MHz operation, while above GHz the correlation increased to well above 20%.

D. Artificial skyrmionic synapses and neurons

An artificial neuron is one of the fundamental computing units in brain-inspired neural networks. To implement the nonlinear neuron activation function, various designs using standard CMOS have been proposed. These CMOS-based artificial neurons typically consist of a large number of transistors, which require a large area and power consumption. Skyrmions can provide an alternative to efficiently implement neuronal behavior. In a nervous system, synapses carry out the role of passing electrical or chemical signal signals between neurons. One of the main characteristics of biological synapses is the synaptic weights which are no longer binary. Such initiation, potentiation, and depression behavior are easy to realize in software but harder to implement in digital CMOS-based circuits.

Various methods have been proposed to implement synapses and neurons using skyrmions [Fig. 14(a)]. One approach is using a defect/notch in the racetrack. The notch acts as an energy barrier, which a skyrmion or domain wall needs to climb over to pass through. For the initiation mode, skyrmions are nucleated and trapped behind the energy barrier of the notch. For the potentiation mode, a large enough current propels the skyrmions past the defect. This behavior mimics the integrate-and-fire behavior of neurons. In the depression mode, the skyrmions are in the postsynapse area, and a current is applied that is opposite to the current direction used for potentiation mode. The skyrmions then get moved back from the postsynapse area to the presyanpse area.[145] The synaptic weight for each mode (potentiation or depression) is determined by the population of skyrmions in the presyanptic or postsynaptic areas. Other variations of this approach have been

used to mimic integrate-and-fire neurons.[146,147] The role of notches in this proposed devices is similar to the notches described earlier in Sec. III E. Results from micromagnetic simulations show up to 98% accuracy for the proposed device.
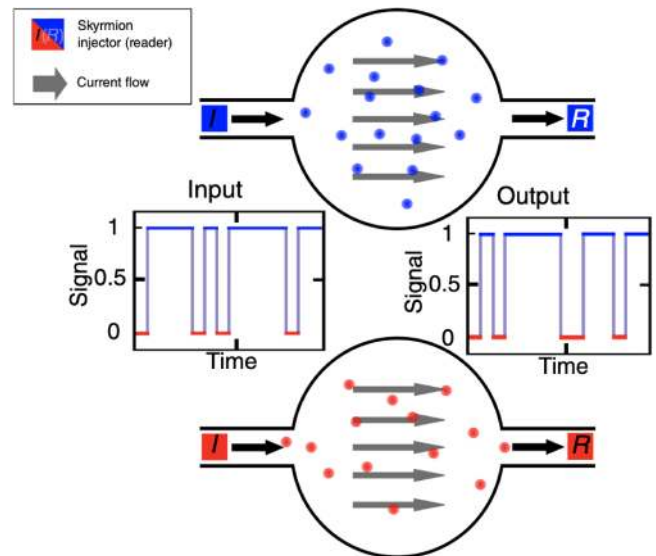

FIG. 13. The proposed device consists of two magnetic chambers into which skyrmions are injected depending on the state of an input telegraph noise signal. The net drift of the skyrmion particles due to a constant current flow along with the thermal diffusion in the chambers leads to an exit order that can be significantly different from that of entry. This behavior is employed to reconstruct a new outgoing signal with the same statistical properties as the first, as well as being uncorrelated from it. Reprinted with permission from Pinna *et al.*, Phys. Rev. Appl. **9**, 064018, 2018. Copyright 2018 American Physical Society.[142]
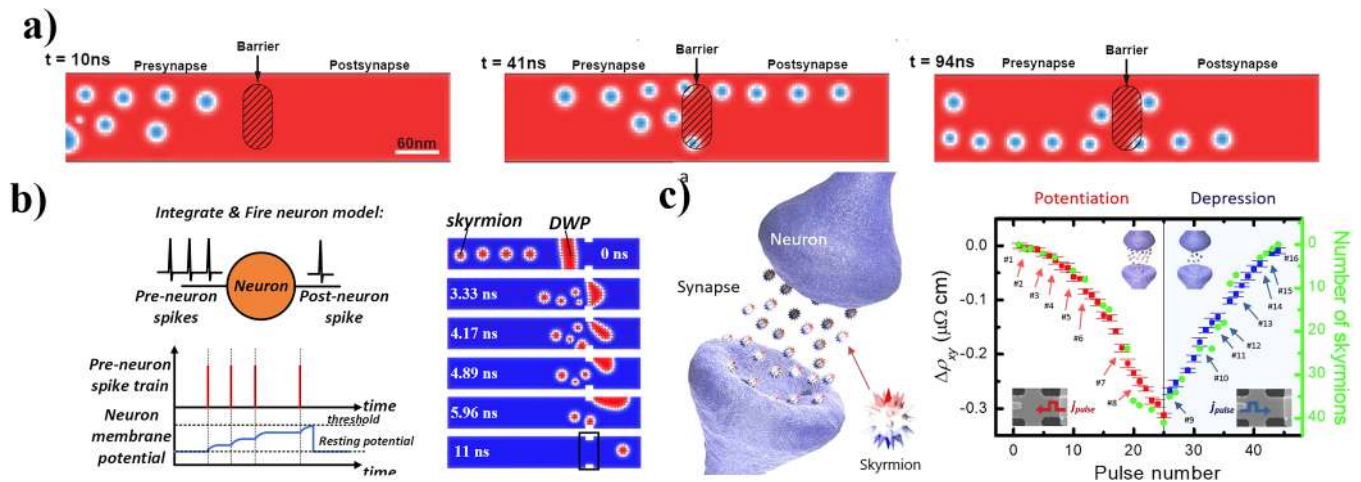
FIG. 14. (a) The synapse proposed using a barrier in the middle of the racetrack. In the initialization mode, skyrmions are nucleated to populate the presynapse section. In the potentiation mode, skyrmions are pushed past the barrier, which results in a sudden change in the skyrmion population in the postsynapse area. Reproduced with permission from Huang *et al.*, Nanotechnology **28**, 08LT02 (2017). Copyright 2017 IOP Publishing. (b) A proposed skyrmion-based neuron. In this case, notches provide the barrier for the domain wall. As the number of skyrmion behind the domain wall increases (presynapse area), their dipole-dipole interaction with the domain wall increases. When the number of skyrmions which is based on the number of spikes, reaches a certain value, the skyrmion and domain wall can pass the notch.[146] (c) The experimental realization of a skyrmion-based synapse, in this model, in the potentiation mode, for each spike, a nucleation current pulse is applied, which nucleates skyrmions and populates the racetrack. For the depression mode, for each applied current, pulse skyrmions get annihilated, which depopulates the racetrack. Reproduced with permission from Song *et al.*, Nat. Electron **3**, 148–155 (2020). Copyright 2020 Nature Publishing Group.

The accuracy of skyrmion-based synapse was reported to be 89% in experiments, as compared to 94% from software simulation of the synapse.[94] Clearly, more work needs to be done to make such devices competitive.

E. High density reservoir computing using skyrmions

Reservoir computing is a paradigm that intersects neural networks, dynamical systems, state-space filters, and random networks. Its central entity is a "reservoir," which is a collection of sparsely and randomly connected neurons (i.e., units with non-linear activation functions) with recurrence, i.e., potentially many feedback paths [Fig. 15(a)]. Reservoir computing has been developed in two flavors independently, viz., the echo-state network (ESN) and liquid state machines (LSM). The essential difference between the two modes is that ESN works with continuous signals, akin to conventional artificial neural networks, while LSM works with spiking signals similar to biological neural networks and is proposed as a biological model of autonomous multi-scale learning.

Reservoir computing provides spatiotemporal inferencing capabilities,[148] i.e., it deals with data that spans both space and time domains (e.g., a video or multi-dimensional biological signal like EEG). Its recurrent nature allows for an input signal sent into the reservoir to propagate through the network at various speeds and activate the neurons at differing times. This enables developing spatiotemporal correlations. Signals from the "past" get correlated with the "present" because the "echo" or the signature of the input signal persists within the reservoir and is evident in its state vector. By sampling these states, it is possible to make inferences about the

input signal both spatially as well as temporally. The learning aspect in reservoir computing arises in the readout operation of the reservoir, which is generally a linear weighted sampler over the reservoir state vector (i.e., a list of activation or non-activation of the reservoir units at any given time). We can train the sampler weights over the reservoir states to make a particular inference. We can also attach multiple different samplers to obtain multiple inferences since the reservoir remains unperturbed by a readout process. It should be noted, in reservoir computing, the interconnections within the reservoir themselves are not tuned or modified, unlike other models of recurrent neural networks such as GRU or LSTMs, which allow for easy one-shot learning approaches similar to extreme learning machines.

In Refs. 149 and 150, authors propose to exploit extended skyrmion textures or fabrics such as skyrmion lattices or stripe states on a magnetic film [Figs. 15(b) and 15(c)] as the reservoir, while the readout or sampling is performed by measuring non-linear interaction between the randomized skyrmionic texture and the current through the film via the anisotropic magnetoresistive (AMR) effect. The current flows through the path of least resistance along the various domain walls in the disordered self-organized domain structure [Fig. 15(d)]. This plays the same role as an input signal propagating through a random reservoir via multiple paths. The skyrmionic texture can also be modified by the applied current, which plays the role of an input signal changing the state of the reservoir.

Such a skyrmion fabric can potentially host a very large density of closely packed interacting reservoir nodes whose dynamics and evolution are determined by the interplay between exchange, DMI, dipolar, thermal interactions, and an applied input current, thus
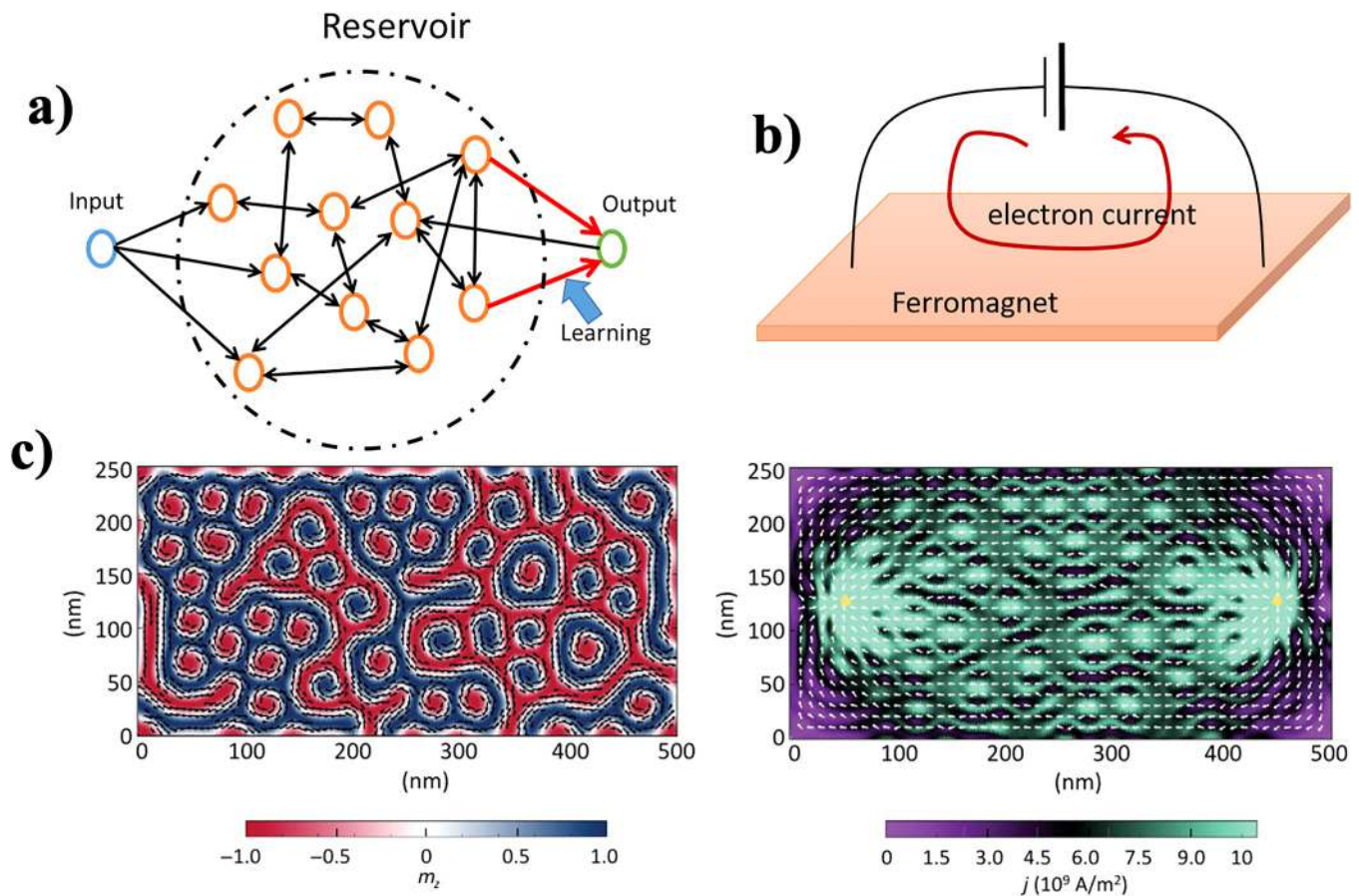
FIG. 15. (a) General schematic of a reservoir computer, which consists of randomly, sparsely, and recurrently connected non-linear activation units. The input signal is imposed on the reservoir, while the output is developed by sampling the reservoir states. Only the output is adjusted during the learning process. (b) Schematic of skyrmion fabric-based reservoir computer. The ferromagnet hosts multiple skyrmions and stripe phases, and the output of the reservoir is obtained by measuring the resistivity of the film, which changes depending on the skyrmion texture due to the anisotropic magnetoresistance (AMR) effect. (c) Simulation of a skyrmion texture (left panel) and current flow (right panel) through it. Reproduced with permission from Bourianoff et al., AIP Adv. 8, 055602 (2018). Copyright 2018 AIP Publishing LLC.

eliminating the area expense of laying down a complex pattern of interconnections between different nodes of the reservoir, if they are built from discrete elements. While initial simulation studies show promising results, practical engineering challenges of readability and distinguishability of reservoir states through the AMR effect could prove to be the major hurdle toward a feasible design and implementation.

F. Skyrmion based high frequency spintronic oscillators

Spintronic oscillators use the built-in precession or gyration of a magnetic state to build an oscillator. This motion can then be detected through the magneto-resistive effect, typically using MTJs. Most commonly used spintronic oscillators employ either spin-transfer or spin–orbit torques along with a magnetic field to generate two compensating torques that do not allow the free layer

magnet to relax into one of its stable states. The frequency of oscillation of such devices is highly tunable, which makes them a great candidate for ultra-small and versatile frequency sources. However, these spin-torque nano oscillators (STNOs) suffer from high phase noise and large linewidths primarily due to their small volumes and non-deterministic multi-domain behavior.

One potential solution to such problems is the use of a controlled multi-domain magnetic texture such as a skyrmion and its gyration around an axis to build an oscillator.[151,152] In these structures, the skyrmion exists on an extended nano-disk where it can gyrate around the central geometric axis [Fig. 16(a)]. The spin–torque pushes the skyrmion toward the boundary in this geometry while the boundaries repel them. As a result, the skyrmion moves along stable circular boundaries of the nano-disk under the spin-torque drive. By placing a small MTJ based reader that covers only the part of the nano-disk, it is possible to read out an oscillatory electrical response [Fig. 16(b)].
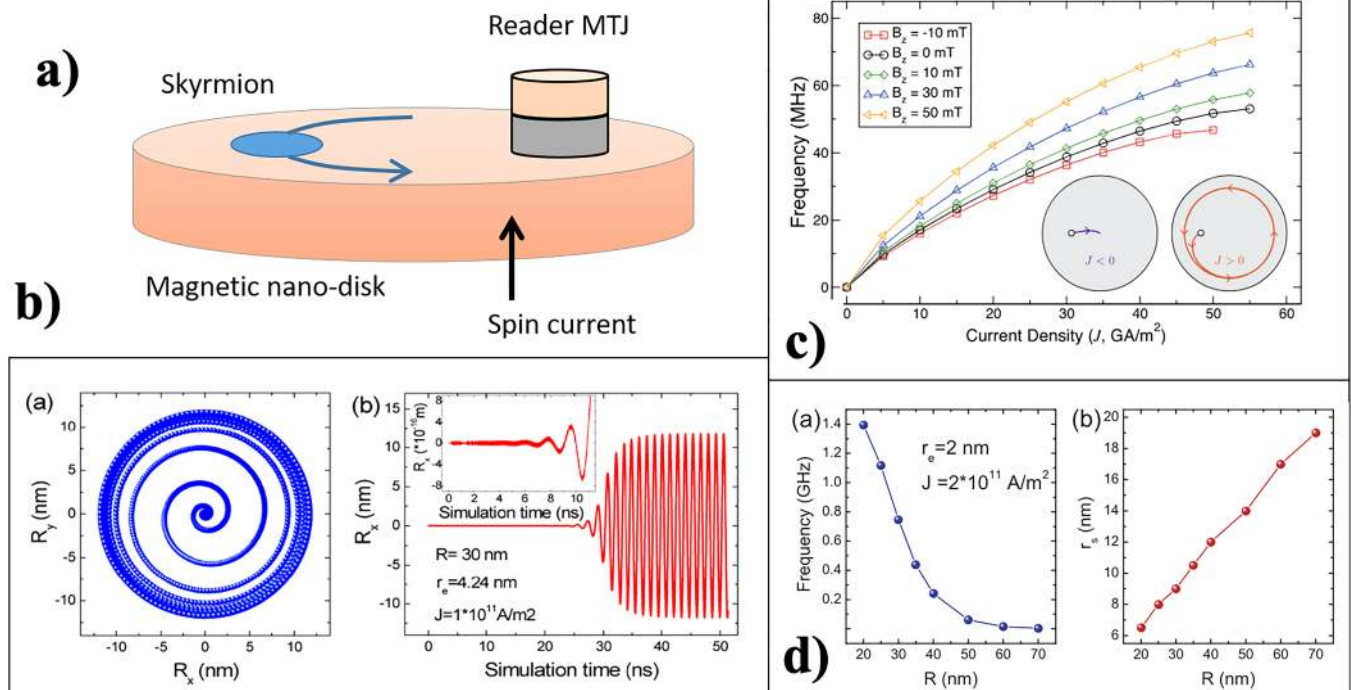
FIG. 16. (a) Schematic of a skyrmionic nano-oscillator (SkNO). Skyrmions are placed in a wide nano-disk, whereupon applying a spin torque through the injection of a spin current drives the skyrmion in a circular orbit through the disk. The readout is done through a small MTJ structure placed on the nano-disk, which samples the skyrmion every period of the gyration orbit. (b) Simulation showing the trajectory of the skyrmion on the nano-disk and the motion through the x-axis (from Ref. 151). (c) Dependence on the central oscillation frequency with current density for various applied magnetic field strength [Garcia-Sanchez et al., New J. Phys. **18**, 075011 (2016). Copyright 2016 Author(s), licensed under a Creative Commons Attribution (CC BY) license]. (d) Dependence of the central oscillation frequency with the nano-disk radius, given a fixed current density and (left panel) injection point contact radius and (right panel) skyrmion radius (b) and (d) from Zhang et al., New J. Phys. **17**, 023061 (2015). Copyright 2016 Author(s), licensed under a Creative Commons Attribution (CC BY) license.151

The frequency of oscillation of the skyrmionic nano-oscillator depends on not only the magnitude of the driving spin-torque [Fig. 16(c)] but also the skyrmion size, nano-disk radius [Fig. 16(d)], and the drive current, providing a rich phase space for oscillator design. It was also reported in Ref. 151 that the linewidth was less than a 1 MHz with a central frequency of nearly 800 MHz, whereas Garcia-Sanchez et al.152 reported a somewhat lower center frequency of a few 100s of MHz. Analysis from both papers indicated that skyrmion motion could be fairly robust against moderate disorders such as grain structure of the magnetic nano-disk and other imperfections such as bubbles, dots, and notches. Using additional skyrmions on the nano-disk can increase the frequency to more than 1 GHz by reading these multiple skyrmions in a single gyration.151

V. TECHNOLOGY CHALLENGES

On the road toward reliable low cost and energy-efficient skyrmionics, there are many challenges. Depending on the target application, they can be of varying importance. For conservative memory or logic based on shuttling skyrmions around, such as our aforementioned temporal memory and other Boolean computing ideas,153 any nucleation of skyrmions needs to be deterministic both in position and in number. On the other hand, stochastic applications such as skyrmion reshufflers are not sensitive to the position and quantity of nucleated skyrmions, although they could be sensitive to other aspects such as the rate of nucleation. Regardless of the precise application, we can identify some common challenges relating to overhead cost and integrability, readability, stability, gateability, and nucleation/annihilation.

To start with, the energy advantage of a skyrmionic circuit (for that matter, any computing paradigm) needs to be evaluated in totality, including the control and read circuitry. As pointed out near the introduction, the bulk of the energy bottleneck with magnetic devices lies in the overhead. We saw that with our temporal memory analysis (Sec. IV B), where the energy consumed in the racetrack was ≪10 fJ, while that in the CMOS transistors used to turn the currents on and off consumed ∼1 pJ. While the dominance of the overhead is perhaps unavoidable with electronic interfaces, the opportunity could very well lie in our ability to map a compact skyrmionic architecture with a particular algorithm its underlying physics naturally accelerates, such as its tunable linear dynamics for analog computing. Such a mapping could significantly reduce the electronic overhead (e.g., eight transistors for wavefront memory vs hundreds for a CMOS-only layout).

Driveability will also require an optimized material thickness that allows long lifetimes and thermal stability, while also providing adequate interfacial DMI and SOT coefficients. This also means we need to evaluate the compatibility of the various components—for instance, impedance matching between the transistors and the heavy metal underlayers, or the ability for these transistors to provide adequate drive current or voltage (e.g., some of the logic applications need ∼2 V VCMA gating, more than the nominal voltage of a 180 nm transistor).

Adequate drivability requires an electronic read unit to detect skyrmions for each logic operation. This in itself is challenging given the small footprint of a skyrmion relative to an MTJ, exacerbated in ferrimagnets. Moreover, after reading the data, an amplifier will be needed to have a reliable output resulting in extra energy and area overhead.

As with many emerging technologies, appropriate gate design for suitable electrostatic or anisotropy control, as well as material integration (channel, oxide, and heavy metal), will need to be perfected. Some of the logic setups rely on precise gate synchronization of skyrmion arrival times, which can be challenging in presence of thermal fluctuations and diffusion. A non-uniform defect density can alter the arrival sequence in a temporal memory device or change the output in a two-lane AND–OR device. In Fig. 11, we have assumed two-input gates, so the geometry needs to be altered for a larger number of inputs to avoid cascading, that can become prohibitively costly. On the other hand, altering device geometry may result in reliability issues. In such circumstances, it may be worthwhile to pay the cost penalty rather than playing with the device geometry that can compromise reliability. Energy, delay and reliability form a triad whose elements can be traded-off against each other depending on specific application thresholds.

Finally, reliable nucleation of skyrmions will be an issue for all non-stochastic devices, especially ones that rely on re-nucleating skyrmions rather than reshuffling them around. Reliable nucleation maybe less relevant for stochastic computing applications depending on their error thresholds. For reshuffler-based applications (Fig. 13), a synchronization between the speeds of injection, nucleation, and expulsion needs to be ensured to avoid bottlenecks that can delay the overall performance by a handsome margin and hamper its reliability. There are other considerations—for instance, higher current densities might enforce higher degrees of correlation among bitstreams, which stochastic computing seeks to avoid. Let us now discuss how we may address some of these challenges.

A. Readability

To use skyrmions or DWs in a digital circuit, we need to be able to electrically detect these magnetic excitations. The most practical method for detecting isolated skyrmions is using MTJs. When a skyrmion or DW reaches an MTJ, the corresponding tunnel magnetoresistance (TMR) generates an output voltage swing which needs to be amplified to get a 0/1 in the output node of the circuit. In order to have a large enough voltage swing without any erroneous electrical detection, the TMR needs to be quite large, 50% in our proposed race logic and reconfigurable hardware applications. Owing to the small size and chiral spin texture of skyrmions, the effective TMR is set by an overall filling factor and can

be significantly smaller than the TMR for a magnetic pillar. For a skyrmion of the same size as the MTJ, this fill factor can be as small as 30% [$TMR_{effective} = $ (fill factor) × TMR]. The TMR can be smaller for ferrimagnets or antiferromagnets as the two sub-lattice spins can oppose each other. TMR ratios of above 100 have been theoretically predicted for antiferromagnets,[154,155] but so far no experiment has demonstrated large TMR ratios for AFMs. The anisotropic magnetoresistance (AMR), varying with applied current density j_c as $\sim (\mathbf{m} \cdot \mathbf{j_c})^2$, has also been investigated for canted magnetic structures including skyrmions,[155] and predicted to rise above 100 percent magnetoresistance (MR) ratio,[156] though a room temperature experimental demonstration is as yet unavailable. Multilayer spin valve structures with synthetic antiferromagnet (SAF) or an intermediate ferromagnetic layer[157,158] are other possibilities. By tuning the bias voltage and reference resistance of the read unit, erroneous data detection seems preventable at a somewhat low effective TMR (∼50%), but the circuit might not be robust enough against variations. In a synchronously clocked system, perhaps where notches quantize the racetrack in the magnetic substrate, a more sensitive detection mechanism like a Pre-Charged Sense Amplifier (PCSA)[159] could be adopted if indeed very low effective TMR becomes a persistent problem.

An alternate way to detect a skyrmion is to look for chiral signatures in a Hall measurement. In magnetic materials there are three components to the transverse resistivity, $\rho_{xy} = \rho_{xy}^{OHE} + \rho_{xy}^{AHE} + \rho_{xy}^{THE}$. The first one, ρ_{xy}^{OHE}, is the ordinary Hall effect (OHE). The second one, ρ_{xy}^{AHE} proportional to the out-of-plane magnetization m_z, is the anomalous Hall effect (AHE). The last one, the topological Hall effect (THE), is induced by the skyrmion's chiral spin texture. THE, is reported to be dominant in B20 skyrmion lattices, but for isolated skyrmions, the AHE becomes the dominant contribution to the transverse Hall resistivity. The magnitude of ρ_{xy} is small for a single skyrmion, but for a larger number of skyrmions, it can have the necessary voltage swing for it to be useful in an electrical circuit. The $\Delta \rho_{xy}$ reported for a single skyrmion can be as small as 3.5 ± 0.5 $n\Omega$-cm for sub-100 nm skyrmions in racetrack width of 1 μm.[160] For a current density of 1 TA m^{-2} and width of 1 μm, the voltage swing would be 3.5 mV.

B. Deterministic nucleation/annihilation

As we discussed in Sec. III C, there are multiple mechanisms available to nucleate and annihilate skyrmions, ranging from external magnetic fields to current pulses to defect sites with locally reduced magnetic anisotropy.[51] The challenge, however, is to make this deterministic, since the methods discussed can lead to inadvertent nucleation of multiple skyrmions.[56,160] Moreover, the position of the nucleated skyrmions needs to be deterministic,[92] meaning that the pinning sites for skyrmion nucleation need to be controlled. For applications where single skyrmions are used to encode data,[123,130,133] the unpredictability of location or number of skyrmions would make the device unworkable. One way around is to design the device so that it can be conservative in the number of skyrmions,[123,153] meaning there is no need for annihilation in the first place. The benefit of conservative devices is that the skyrmions can be pre-fabricated in a controlled environment. It is also important to avoid added nucleation. Current pulses of magnitude above

$j_c \approx 10^{12}$ A/m^2 are typically used to nucleate skyrmions, in fact, even a bit lower sometimes due to thermal effects.[92,95] This means the operational current, j of the device, needs to be well below the nucleation/annihilation limit. On the other hand, the current has to be large enough to unpin the skyrmion. For the applications where the density of skyrmions is important, for example, neuromorphic applications,[144] the deterministic nucleation/annihilation of individual skyrmions would influence the ratio at which they are created or deleted, and thus the overall probability of ones and zeros. This would also be sensitive to the magnitude of current density and defects.

In addition to deterministic challenges, skyrmion nucleation can be energetically costly,[161] as the current pulse I_n for nucleation needs to be larger than the driving current I_d. The power consumption would be $(I_n/I_d)^2$ times higher, which combined with nucleation time would make each creation/annihilation process energy-hungry, arguing for a conservative design that shuttles rather than creates/destroys skyrmions repeatedly. Our pulse duration studies discussed in Sec. III C place the nucleation time at ∼1–10 ns, comparable to drive time. Reference 95 uses a current pulse of 10^{12} A m^{-2} over 6 ns for nucleation, while the drive time we estimated for race logic across a 640 nm racetrack was under 10 ns. Reusing pre-fabricated skyrmions would make the recovery operation in race logic 1-2 orders of magnitude more energy-efficient than nucleating skyrmions each cycle.

C. Positional stability

Large skyrmions generally have larger lifetimes and more diffusion, while small ones get easily pinned by defects and go through a thermally activated creep regime in transport. The amount of diffusion needs to be tightly restricted to service the needs of a given technology (Table III). In order to ensure the reliability of the magnetic memory, pinning sites need to be engineered lithographically. The pinning energy barrier needs to be large enough to stabilize skyrmion location and, depending on the application, similar to the lifetime energy barrier, around 30 to 50 $k_B T$. Much like the lifetime, there is a trade-off between having adequate skyrmion stability (higher barriers) vs modest drive currents that can unpin and move them efficiently without blowing up the energy budget, crashing them into the sidewalls, or otherwise annihilating them in the process. In addition, if the driving current is too large, it can nucleate unwanted skyrmions. In the case of domain walls, similar positional stability is needed, but unavoidable lithographic edge roughness can cause significant DW pinning in the racetrack. Controlling the amount of pinning for skyrmions might be easier to achieve as they can avoid edges, implying a distinct advantage in terms of material engineering.

D. Integration challenge

The magnetic racetracks need to be integrated with silicon CMOS transistors that constitute the control circuitry for memory/logic applications. The difficulty in designing a high-speed skyrmionic device is the large current needed to move the skyrmion at high speed. Due to the impedance mismatch between the heavy metal underlayer and CMOS control circuitry, only a tiny fraction of current is fed to the racetrack, limiting our scope for supply

voltage reduction. Using larger transistors will reduce their resistance, allowing a high drive current. Since the control circuitry consumes the bulk portion of the overall energy (Fig. 10),[123] the reduction of transistor resistance will reduce the overall energy consumption by balancing the impedance between the racetrack and the circuitry, allowing higher frequency operation enabled by higher skyrmion speeds, albeit with an associated area overhead for the larger transistors.

For conventional racetrack memories, the energy consumption ratio between the CMOS and the racetrack underlayer will depend on the number of skyrmions in the racetrack and the number of read stacks placed on the racetrack. As the applied current to the racetrack underlayer will move all the skyrmions present in the racetrack, the driving energy consumption ratio of CMOS/racetrack will be lower for a higher number of skyrmions in a racetrack. Thus, longer racetracks and a higher number of small-sized skyrmions will lower energy consumption. However, smaller skyrmions are harder to detect, and longer wires are more susceptible to noise, creating erroneous output. Thus, to achieve energy efficiency without affecting reliability (a trade-off we emphasized near the start of this article), choosing the optimal racetrack length and skyrmion size will be vital. However, it is worth mentioning that the skyrmion nucleation energy will be a deciding factor of the overall energy consumption for the conventional multi-skyrmion racetrack memory.

There is also an issue of current sharing between metallic magnets with the heavy metal underlayer, which can be mitigated by using insulating magnetic oxides such as spinels and ferrites. The physics gets considerably more involved in antiferromagnetic spin dynamics which has added inertial terms and will need to be explicitly re-evaluated for skyrmion transport.

E. Speed stability

As was mentioned in Sec. I C, skyrmions need to be fast while requiring a small drive current to guarantee energy efficiency. Besides energy efficiency constraints, we get two limits on the current range. As seen in Fig. 5, too large a drive current can distort and dissolve the skyrmions and create overall nonlinearity, which sets the upper limit. On the other hand, the minimum current must be sufficient to unpin skyrmions away from engineered pinning sites and thus set by the required positional lifetime of the skyrmions.

VI. SUMMARY/OUTLOOK

Recent experiments have unearthed a wealth of solitonic excitations in thin magnets, from skyrmions to skyrmioniums and chiral bobbers.[162] What makes these entities interesting is that they can be scaled down to fairly small sizes through material engineering, utilizing their topological barriers that work effectively against thermal fluctuations, especially if the sizes are not too small. Topology also covers their dynamical properties as these excitations can work around defects by distorting their shapes at low current densities. The size scaling offers distinct advantages relating to high-density information encoding that can be challenging to accomplish with conventional magnets. Their quasi-linear current-driven motion and tunable properties would allow certain applications such as temporal racetrack memory for low-density

skyrmions, while in low current thermally diffusive setups, they could act as decorrelators.

There are, however, cautionary lessons, as the topological protection is not absolute. The energy barrier for small isolated metastable skyrmions in thin films can be small, while thicker films tend to make drivability challenging. While topology also offers some dynamical resilience, it comes at the cost of added topological damping, Magnus force, and overall slowdown compared to domain walls at large current densities. Finally, device applications need to be carefully evaluated for the entire circuit, including individual overhead costs for acceptable electronic read–write–erase–recovery operations.

Key milestones along this path will include managing the energy cost and predictability of skyrmion nucleation, adequate TMR across MTJs, and both static (lifetime) and dynamic (positional) stability at room temperature. Key experiments along these lines will need to be executed, demonstrating projected lifetimes $\sim$ days or years for $\sim 10-20$ nm skyrmions, adequate positional localization (Table III) with controlled diffusion or pinning along a racetrack (Fig. 8), subsequent release with temporal wavefront arrival under modest current densities $\sim 10^{11}$ A/m^2 over <10 ns, as well as successful read (effective TMR including skyrmion shape function $>50\%$), recovery, and reset (coordinate erase), in order to capitalize on the intrinsic strengths of these topologically protected computing bits.

SUPPLEMENTARY MATERIAL

See the supplementary material for the list of experimentally feasible ferrimagnetic Heusler candidates.

ACKNOWLEDGMENTS

DATA AVAILABILITY

The data that support the findings of this study are available from the corresponding author upon reasonable request.

APPENDIX A: SKYRMION TOPOLOGY AND POINCARÉ MAP CLASSIFICATION

Alternative to the energy arguments in the text the skyrmion winding number N_{sk} and domain angle ψ can be derived from analysis of the Poincaré diagrams for DMI vector field. N_{sk} sets both the exchange E_{ex} and the symmetry breaking DMI E_{DMI} energy barriers [Eq. (B6)] that generate the requisite spin winding against the background spin distribution. A convenient way to see the topological classifications of skyrmions arising from different forms of the DMI is by plotting a 2D cross sectional cut in the x–y plane. The different skyrmionic forms map onto the well known classifications of linear systems (Fig. 1), summarized by stable solutions to the 2D differential equation set $\frac{d}{dt}\begin{pmatrix} x \\ y \end{pmatrix} = A \begin{pmatrix} x \\ y \end{pmatrix}$, where t

is a parameter that takes us along a solution curve. The shapes of the curves are set by the Trace (tr) and Determinant (det) of the matrix A and can be plotted as so-called Poincaré diagrams[34]—for instance, stars (tr$^2 = 4$ det > 0) that map onto Néel skyrmions, limit cycles (det > 0, tr $= 0$) that map onto Bloch skyrmions, spirals ($0 < $ tr$^2 < 4$ det) that map onto a combination of Néel and Bloch, and saddle points (det < 0) that map onto antiskyrmions.

For skyrmions stabilized by DMI set by the crystal structure, the symmetry breaking energy connecting two spins $S_{i,j}$ takes the form

$$E_{DMI} = \boldsymbol{D}.(\boldsymbol{S}_i \times \boldsymbol{S}_j), \tag{A1}$$

with

$$\boldsymbol{D} = \begin{cases} \hat{z} \times \boldsymbol{r}_{ij} & \text{Interfacial,} \\ \boldsymbol{r}_{ij} & \text{B20,} \\ \sigma_z.\boldsymbol{r}_{ij} & D_{2d}. \end{cases} \tag{A2}$$

The first is set by a symmetry breaking field perpendicular to the interface between a heavy nonmagnetic metal and a magnetic film, the second is aligned within a non-centrosymmetric magnet between the spin carrying atoms, and the third by the elongation of the magnetic unit cell along with the $\hat{y}$-direction. The vector field for the $\boldsymbol{D}$ can then be rewritten in 2D as

$$\boldsymbol{D} = \begin{cases} \pm \begin{pmatrix} -y \\ x \end{pmatrix} & \text{Interfacial, Néel skyrmions,} \\ \pm \begin{pmatrix} x \\ y \end{pmatrix} & \text{B20, Bloch skyrmions,} \\ \pm \begin{pmatrix} x \\ -y \end{pmatrix} & D_{2d}, \text{ antiskyrmion.} \end{cases} \tag{A3}$$

From the E_{DMI} in order to get lowest DMI energy, the vector field of each $\boldsymbol{S}$ must be in a plane perpendicular to $\boldsymbol{D}$ so that $\boldsymbol{S}_i \times \boldsymbol{S}_j$ is parallel/antiparallel to $\boldsymbol{D}_\perp$, the vector perpendicular to the DMI vector $\boldsymbol{D}$,

$$\frac{d}{dt}\begin{pmatrix} x \\ y \end{pmatrix} = \boldsymbol{D}_\perp = \begin{cases} \pm \begin{pmatrix} x \\ y \end{pmatrix} & \text{Néel,} \\ \pm \begin{pmatrix} -y \\ x \end{pmatrix} & \text{Bloch,} \\ \pm \begin{pmatrix} y \\ x \end{pmatrix} & \text{antiskyrmion.} \end{cases} \tag{A4}$$

This would give A in our linear systems classification as

$$A = \begin{cases} \pm \begin{pmatrix} 1 & 0 \\ 0 & 1 \end{pmatrix} & \text{Néel,} \\ \pm \begin{pmatrix} 0 & -1 \\ 1 & 0 \end{pmatrix} & \text{Bloch,} \\ \pm \begin{pmatrix} 0 & 1 \\ 1 & 0 \end{pmatrix} & \text{antiskyrmion,} \end{cases} \tag{A5}$$

whose traces and determinants satisfy the 2D Poincaré diagram classification rules above.

We can quantify the winding of spins around the skyrmion with the winding number N_{sk} introduced earlier (Sec. I C). An electron moving around a closed loop on the Fermi surface picks up a geometrical Berry phase related to the solid angle subtended at the center of the Fermi sphere, similar to the precession of a Foucault pendulum. This phase is given by the flux of the magnetic field in the k-space, $\phi_n = \oint \vec{B}_k \cdot d\vec{S}_k$, $\vec{B}_k = \vec{\nabla}_k \times \vec{A}_k$, $\vec{A}_k = iu_k^* \vec{\nabla}_k u_k$, where u_k is the Bloch part of the electron wavefunction. For magnets, the corresponding phase space $k \to m$, where m is the normalized magnetic moment. We use a standard 2×1 spinor representation $u_m = \begin{pmatrix} \exp[-i\Psi/2]\cos\theta/2 \\ \exp[i\Psi/2]\sin\theta/2 \end{pmatrix}$. The corresponding magnetic field then maps onto a magnetic monopole while the Chern number is set by the quantum of the Berry flux, $C_n = \phi_n/2\pi$; 2D C_n simplifies to N_{sk}.

APPENDIX B: SKYRMION ENERGY TERMS

In a 1D continuum representation, the width of a domain wall arises from a competition between exchange stiffness A_{ex} and uniaxial anisotropy K_u. Taking into account only the first two energy terms, we get the energy per unit area

$$E' = t_F \int_{-\infty}^{\infty} dx[A_{ex}(d\theta/dx)^2 - K_u \cos^2\theta]. \tag{B1}$$

Minimizing this energy, i.e., invoking Euler–Lagrange's equations, leads to the differential equation

$$\frac{d^2\theta}{dx^2} = \frac{\sin\theta\cos\theta}{\Delta_0^2}, \tag{B2}$$

where $\Delta_0 = \sqrt{A_{ex}/K_u}$ is the domain wall width (exchange wants to spread the spins around, uniaxial anisotropy wants to align them). Solving this equation with boundary conditions $d\theta/dx|_{x=\infty} = 0$ gives us the equation for a 1D domain wall as $\theta(x) = 2\tan^{-1}\left[e^{(x-x_0)/\Delta_0}\right]$ spread over a thickness Δ_0 around the position x_0. We can then approximate the various integrals per unit area as

$$E'_{ex} = t_F \int_{-\infty}^{\infty} dx A_{ex}(d\theta/dx)^2 = 2A_{ex}/\Delta_0,$$
$$E'_{ani} = t_F K_u \int_{-\infty}^{\infty} dx \sin^2\theta = 2K_u\Delta_0, \tag{B3}$$

where we used the differential equation above to replace one $d\theta/dx = \sin\theta/\Delta_0$ term in each of the first two integrals. We can also calculate the 1D equivalent of a chiral DMI energy as

$$E'_{DMI} = -t_F \sin\psi_0 D \int_{-\infty}^{\infty} dx d\theta/dx = -\pi t_F D \sin\psi_0, \tag{B4}$$

where ψ_0 is the domain wall angle, $\psi_0 = 0$ is a Bloch domain wall, and $\psi_0 = \pi/2$ is a Néel domain wall. The full 3D form of Eq. (B1) with DMI corrections should be taken into account to describe 2D skyrmions. Writing $\mathbf{m}$ in spherical cooirdnates, $\mathbf{m} = (\sin\theta\cos\psi,$

$\sin\theta\sin\psi, \cos\theta)$ and using Euler–Lagrange's equation, the solutions for $\theta(r)$ can be approximated as two opposing domain walls at antipodal locations,

$$\theta(r) = 2\tan^{-1}\left[\frac{\sinh(R_{sk}/\Delta)}{\sinh(r/\Delta)}\right], \tag{B5}$$

where R_{sk} is the radius of the core. Substituting this form, we can evaluate all the energy integrals[36–38]

$$E_{ex} = (2\pi A_{ex} t_F)\left(\frac{2R_{sk}}{\Delta} + \frac{2\Delta}{R_{sk}}N_{sk}^2\right)f_{ex}(\rho),$$
$$E_{DMI} = -(2\pi R_{sk} t_F)\pi D f_{DMI}(\rho),$$
$$E_{ani} = (4\pi K_u t_F)R_{sk}\Delta f_{ani}(\rho),$$
$$E_{Zeeman} = (\pi R_{sk}^2 t_F) \times (2\mu_0 M_S H_z)f_{Zeeman}(\rho), \tag{B6}$$
$$E_{demag} = -(2\pi\mu_0 M_s^2 t_F)R_{sk}\Delta$$
$$\times(f_s(\rho, t_{FM}/\Delta) - \cos\psi^2 f_v(\rho, t_{FM}/\Delta)),$$
$$\text{with} \quad D \equiv (D_{int}\cos\psi - D_{bulk}\sin\psi),$$

where ψ is once again the domain tilt angle. $f_s(\rho, t_{FM}/\Delta)$ and $f_s(\rho, t_{FM}/\Delta)$ are surface and volume demagnetization form factors, respectively. For ultrathin film limit, $t_{FM} \ll \Delta$, R_{skm}, $f_s \simeq f_{ani}$ and f_v can be ignored.[39] The form factors for small size, obtained by fitting numerical simulations, are given by

$$f_{ex}(\rho) \approx \left[1 + 1.93\frac{\rho(\rho - 0.65)}{\rho^2 + 1}e^{-1.48(\rho-0.65)}\right],$$
$$f_{ani}(\rho) \approx \left[1 - \frac{1}{6\rho}e^{-\rho/\sqrt{2}}\right],$$
$$f_{DMI}(\rho) \approx \left[N_{sk} + \frac{1}{2\pi\rho}e^{-\rho}\right], \tag{B7}$$
$$f_{Zeeman}(\rho) \approx \left[1 + \frac{\pi^2}{12\rho^2} - \frac{0.42}{\rho^2}e^{-\rho^2}\right].$$

We have deliberately separated out the large radius expressions, which are easy to understand intuitively (see Fig. 17), times dimensionless form factors that account for the small skyrmion adjustment. Note that even in the large skyrmion expression we get an extra exchange term $\propto N_{sk}^2\Delta/R_{sk}$ relative to a 1D domain wall, that arises exclusively from the angular winding term $N_{sk}\langle\sin^2\theta\rangle/r^2$, i.e., the 2D curvature, integrated between $R_{sk} \pm \Delta$, and replacing once again $\sin\theta \approx \Delta(d\theta/dr)$ when integrating along the radial coordinate.

Collecting terms, we see that for large skyrmions with unit vorticity number $N_{sk} = 1$, we get $E_{ex} \sim 4\pi A_{ex} t_F(R_{sk}/\Delta + \Delta/R_{sk})$, $E_{ani} \sim t_F K_u R_{sk}$ and $E_{DMI} \sim -\pi t_F D(R_{sk} + \Delta)$.
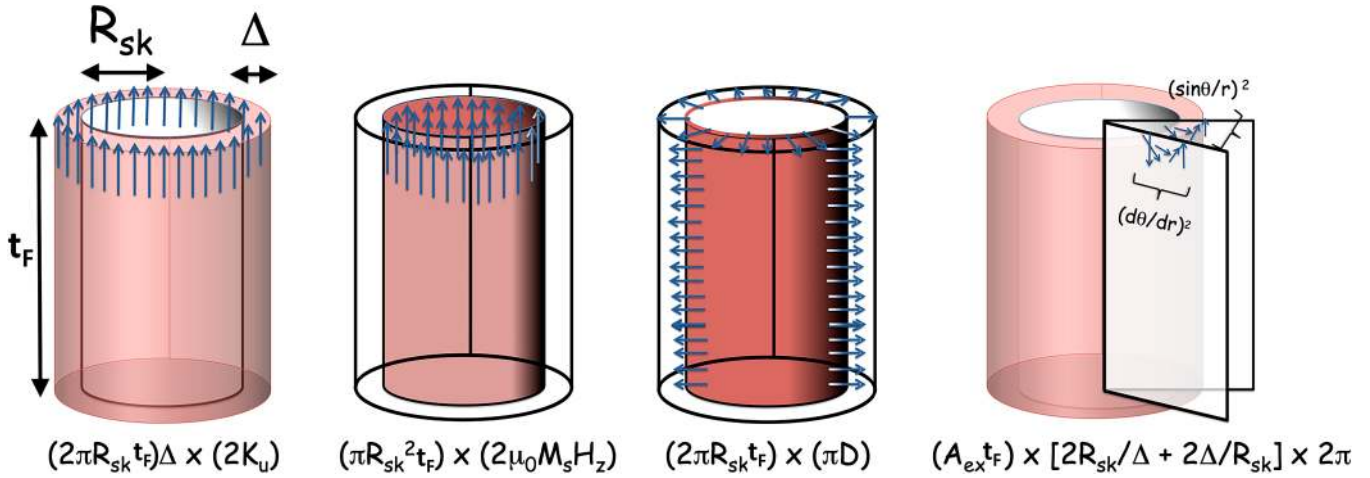
FIG. 17. A schematic view of skyrmion as a cylinder.

We can derive the DMI energy in the continuous limit as

$$
E_{\text{DMI}} = \begin{cases}
D_0 \cos[(N_{sk}-1)\phi + \psi]\left(\partial_r\theta + \dfrac{N_{sk}}{r}\sin\theta\cos\theta\right) \\
\text{(Interfacial DMI, Néel skyrmion),} \\
D_0 \sin[(N_{sk}-1)\phi + \psi]\left(\partial_r\theta + \dfrac{N_{sk}}{r}\sin\theta\cos\theta\right) \\
\text{(B20 bulk DMI, Bloch skyrmion),} \\
D_0 \sin[(N_{sk}+1)\phi + \psi]\left(-\partial_r\theta\cos 2\theta + \dfrac{N_{sk}}{r}\sin\theta\cos\theta\right) \\
\text{(}D_{2d}\text{ DMI, antiskyrmion),}
\end{cases}
\tag{B8}
$$

with $D_0 = 2\pi t_F D$ and t_F the film thickness. The $N_{sk}\sin\theta\cos\theta/r$ term has a much smaller contribution to the energy than the other terms. This would make $N_{sk} > 1$ unfavorable, as the term in exchange energy related to the winding number changes as N_{sk}^2. We can then see from Eq. (B8) that for interfacial and B20 DMI $N_{sk} = 1$ gives the minimum energy with $\psi = 0(\pi)$, $\pi/2(3\pi/2)$, respectively (depending on DMI sign), generating respectively Néel and Bloch skyrmions tha map, respectively, onto nodes and limit cycles in 2D (Fig. 1). For D_{2d} structures, they generate antiskyrmions that map onto saddle points, with $N_{sk} = -1$ and $\psi = \pi/2(3\pi/2)$.

APPENDIX C: DYNAMICS OF SKYRMION AND DWS

Using the Thiele approximation we get the following equation for ith layer in a multi-sublattice magnet[38] for skyrmions

$$
\begin{aligned}
&\boldsymbol{F}_{ex_i} + \Sigma_j F_{ij} + 4\pi N_i t_{F_i} M_{s_i}(\hat{z}\times\boldsymbol{v}_{sk})/\gamma_i \\
&- t_{F_i} M_{s_i}\mathcal{D}.(\alpha\boldsymbol{v}_{Sk})/\gamma_i - \frac{4\hbar}{2q}I\,\theta_{SH}R(\psi)j_{\text{HM}} = 0.
\end{aligned}
\tag{C1}
$$

We have taken current polarization $\boldsymbol{P} = \boldsymbol{j}_{\text{HM}}\times\hat{z}$ to generalize to any $\boldsymbol{j}_{hm}$ direction. $\boldsymbol{F}_{ex_i} = -\mu_0 M_{s_i}\int \boldsymbol{H}_{\text{eff}}\cdot\nabla\boldsymbol{m}$ denotes forces from edges, defects, skyrmion-skyrmion repulsion and varying fields (for

example, anisotropy gradient), and is zero when $\boldsymbol{H}_{\text{eff}}$ is uniform. F_{ij} on the other hand arises from interactions between neighboring layers or sublattices. The third term arises from the inertial term to the right of the LLG equation, with $N_i = \pm 1$ the skyrmion winding number. The fourth term arises from the Gilbert damping term in the LLG equation, and involves $\mathcal{D}$ the dissipation tensor—assumed isotropic with diagonals $\mathcal{D}_{xx}$ set by the dissipation tensor, $\mathcal{D}_{ij} = \int dxdy(\partial_i\boldsymbol{m}\cdot\partial_j\boldsymbol{m})$. For a 2π model this term matches the exchange integral to within a constant [Eq. (B7)], $\mathcal{D}_{xy} = \mathcal{D}_{yx} = 0$, $\mathcal{D}_{xx} \approx R_{sk}/2\Delta\times f_{ex} = \rho f_{ex}(\rho)/2$. γ_i is the gyromagnetic ratio, t_{F_i} is the thickness of sublattice i. f_{ex} is the fitting term coming from the exchange integral. M_{s_i} saturation magnetization of the ith film. The final term arises from the adiabatic spin orbit torque, where $I = \frac{1}{4}I_d(\rho, \Delta)$ is the integral of DMI energy Eq. (B6), $I_d = \int_0^\infty dr[r\partial_r\theta + N_{sk}\sin\theta\cos\theta] = \pi R_{sk}f_{\text{DMI}}$. This integral is, in effect, a shape factor of the skyrmion. $R(\psi) = \begin{pmatrix} \cos\psi & \sin\psi \\ -\sin\psi & \cos\psi \end{pmatrix}$ is the rotation matrix acting on the 2D unit vectors and involves the domain angle ψ ($\psi = 0, \pi$ for Néel skyrmions, $\pm\pi/2$ for Bloch, and in between for hybrid), the current density $\boldsymbol{j}_{\text{HM}}$ in the HM layer assumed to be along the x direction (polarization in $-\hat{y}$ direction). Solving for $\boldsymbol{v}_{sk}$ in absence of external forces and $F_{ij} = -F_{ji}$, we get the equation in the main text Eq. (6). For domain walls we deal with the wall coordinate X and the domain wall angle ψ, setting the skyrmion spin orientation within the rigid skyrmion (Thiele) approximation $\theta(t) = 2\arctan[\exp(x - X(t))/\Delta_0]$. Writing out the LLG equation, and integrating once again over the domain wall coordinate, we get the coupled equations

$$
\frac{d\psi}{dt} + \frac{\alpha_{\text{eff}}}{\Delta_0}\frac{dX}{dt} = \gamma_{\text{eff}}H_a,
\tag{C2}
$$

$$
\frac{dX}{dt} - \Delta_0\alpha_{\text{eff}}\frac{d\psi}{dt} = \Delta_0\gamma_{\text{eff}}(H_D\sin\psi - H_k\sin\psi\cos\psi),
\tag{C3}
$$

where for a two sublattice system with same thickness t_F, $H_a = \pi\hbar\theta_{SH}j_{HM}\cos\psi/4q\mu_0 M_{eff}t_F$, $M_{eff} = M_1(T) - M_2(T)$, $\gamma_{eff} = M_{eff}/(S_1 - S_2)$, $\alpha_{eff} = \alpha(S_1 + S_2)/(S_1 - S_2)$, with $S_i = M_i/\gamma_i$ for the two sub-lattice system. Solving for $dX/dt \equiv v_{DW}$ with $d\psi/dt = 0$ (no precessional motion or Walker breakdown) and $H_D \gg H_K$, we get the Eq. (8) in main text

$$v_{DW} = \frac{\pi}{2}\frac{D_{int}j_{HM}}{\sqrt{(S_0(T)j_{hm})^2 + (\alpha S(T)j_0)^2}}. \quad (C4)$$

Note that with AFMs where $S = 0$, it is theoretically possible for a DW to reach very high speeds. In Eq. (8) $v_{DW} \propto j_{HM}/\alpha$ at high currents and low damping so that in an antiferromagnet the speed would become very large. At that point, the broader assumption of skyrmion or DW rigidity will no longer hold and the structures start to contract, assuming they are still stable energetically. For speeds v'_{DW} comparable to magnon speeds v_m, a Lorentz contraction of domain wall width happens, $\Delta'_0 = \Delta_0\sqrt{1 - (v'_{DW}/v_m)^2}$.[49] Substituting in Eqs. (14) and (15), the speeds become[50]

$$v'_{DW} = v_{DW}\sqrt{1 - (v'_{DW}/v_m)^2}, \quad (C5)$$

where v_{DW} is the non-relativistic DW speed. Similarly for AFM skyrmions the speed is $v_{sk} \propto j_{HM}/\alpha$ high current low damping would be very large. At speeds near magnon speeds,[163] we have to revisit our assumption of circular skyrmions and assume an elliptical shape with the two diameters functionally dependent on the skyrmion speed. We can derive the relativistic corrections using staggered coordinates, set by the Néel vector $\boldsymbol{n} \equiv (\boldsymbol{m_1} - \boldsymbol{m_2})/|\boldsymbol{m_1} - \boldsymbol{m_2}|$,

$$n = (\sin\theta\cos\psi\sin\theta\sin\psi, \cos\theta),$$
$$\theta = 4\tan^{-1}[\exp(\sqrt{X^2 + Y^2})],$$
$$\psi = \tan^{-1}(Y/X), \quad (C6)$$
$$Y = y/D_y,$$
$$X = (x - x(t))/D_x,$$

where D_y and D_x are the majority and minority axial lengths for a skyrmion ellipse. We can break the forces acting on a skyrmion into two categories. Conservative forces derive from a potential gradient and give zero net work when integrated around a closed path ($\oint \nabla U \cdot d\boldsymbol{l} = 0$). In contrast, non-conservative forces such as spin torque and damping can siphon energy in or out of the system all along the closed path and do not sum out to zero. The former is described by a Lagrangian L, the difference between kinetic and potential energy, while the latter is describe by a Rayleigh dissipation density R_0. In staggered coordinates, we write them as

$$L = \frac{a_m}{2}\dot{\boldsymbol{n}}^2 - \frac{A_{AFM}}{2}\Sigma\partial_i\boldsymbol{n}^2 + K/2(n_z)^2$$
$$- \frac{D_{int}}{2}\boldsymbol{n}.[(\hat{\boldsymbol{z}} \times \nabla) \times \boldsymbol{n})], \quad (C7)$$

$$R_0 = \alpha\frac{M_s}{\gamma}\dot{\boldsymbol{n}} + \tau_{sh}(\hat{y} \times \boldsymbol{n}), \quad (C8)$$

where $a_m = (M_s/\gamma)^2\chi$, χ is the magnetic susceptibility, A_{AFM} is the exchange stiffness, K the uniaxial anisotropy, and D_{int} the interfacial DMI. τ_{sh} is the coefficient of the spin orbit torque for current propagating in the $\hat{x}$ direction defined as $\tau_{sh} = \gamma a/t_F = \frac{\gamma\hbar}{2qM_st_F}\theta_{SH}j_{HM}$.

Solving the Euler–Lagrange equation including Rayleigh dissipation, $\frac{\delta L}{\delta q} - \frac{d}{dt}\frac{\delta L}{\delta\dot{q}} + \frac{\delta R_0}{\delta\dot{q}} = 0$, where the generalized coordinate set $q \in \{D_x, D_y, x(t)\}$, and using Eqs. (C6), we get

$$D_x = \frac{D_0}{2}\left[1 + \sqrt{1 - (v_{sk}/v_m)^2}\right], \quad (C9)$$

$$D_y = \frac{D_0}{2}\left[1 + \frac{1}{\sqrt{1 - (v_{sk}/v_m)^2}}\right], \quad (C10)$$

where $D_0 = 2R_{sk}$ is the diameter of a circular skyrmion. We can see that as v_{sk} increases, D_x reduces while D_y increases, and the skyrmion gets more elliptical. For SOT driven skyrmion, we get

$$v'_{sk} = v_{sk}\left[\frac{1 + \sqrt{1 - (v'_{sk}/v_m)^2}}{2}\right]. \quad (C11)$$

The end result is that distortion limits relativistic skyrmions in antiferromagnets to the same bounds that limit 1D domain walls.

REFERENCES

[1]A. D. Kent and D. C. Worledge, Nat. Nanotechnol. **10**, 187 (2015).

[2]L. Thomas, G. Jan, S. Le, S. Serrano-Guisan, Y.-J. Lee, H. Liu, J. Zhu, J. Iwata-Harms, R.-Y. Tong, S. Patel, V. Sundar, D. Shen, Y. Yang, R. He, J. Haq, Z. Teng, V. Lam, P. Liu, Y.-J. Wang, T. Zhong, and P.-K. Wang, in *2017 IEEE SOI-3D-Subthreshold Microelectronics Technology Unified Conference (S3S)* (IEEE, 2017), Vol. 1.

[3]J. M. Slaughter, K. Nagel, R. Whig, S. Deshpande, S. Aggarwal, M. DeHerrera, J. Janesky, M. Lin, H. Chia, M. Hossain, S. Ikegawa, F. Mancoff, G. Shimon, J. Sun, M. Tran, T. Andre, S. Alam, F. Poh, J. Lee, Y. Chow, Y. Jiang, H. Liu, C. Wang, S. Noh, T. Tahmasebi, S. Ye, and D. Shum, in *2017 IEEE International Magnetics Conference (INTERMAG)* (IEEE, 2017), Vol. 1.

[4]M. N. Baibich, J. M. Broto, A. Fert, F. N. Van Dau, F. Petroff, P. Etienne, G. Creuzet, A. Friederich, and J. Chazelas, Phys. Rev. Lett. **61**, 2472 (1988).

[5]G. Binasch, P. Grünberg, F. Saurenbach, and W. Zinn, Phys. Rev. B **39**, 4828 (1989).

[6]J. C. Slonczewski, Phys. Rev. B **39**, 6995 (1989).

[7]J. Slonczewski, J. Magn. Magn. Mater. **159**, L1 (1996).

[8]L. Berger, Phys. Rev. B **54**, 9353 (1996).

[9]S. I. Kiselev, J. C. Sankey, I. N. Krivorotov, N. C. Emley, R. J. Schoelkopf, R. A. Buhrman, and D. C. Ralph, Nature **425**, 380 (2003).

[10]T. Gilbert, IEEE Trans. Magn. **40**, 3443 (2004).

[11]J. P. Kim, T. Kim, W. Hao, H. M. Rao, K. Lee, X. Zhu, X. Li, W. Hsu, S. H. Kang, N. Matt, and N. Yu, in *2011 Symposium on VLSI Circuits—Digest of Technical Papers* (IEEE, 2011), Vol. 296.

[12]Q. Shao, P. Li, L. Liu, H. Yang, S. Fukami, A. Razavi, H. Wu, K. L. Wang, F. Freimuth, Y. Mokrousov, M. D. Stiles, S. Emori, A. Hoffmann, J. Åkerman, K. Roy, J.-P. Wang, S.-H. Yang, K. Garello, and W. Zhang, arXiv:2104.11459 (2021).

[13]Y. Xie, J. Ma, S. Ganguly, and A. W. Ghosh, J. Comput. Electron. **16**, 1201 (2017).

[14]Y. Xie, B. Behin-Aein, and A. W. Ghosh, IEEE Trans. Electron. Devices **64**, 319 (2017).

[15]K. Munira, W. H. Butler, and A. W. Ghosh, IEEE Trans. Electron. Devices **59**, 2221 (2012).

[16]J. Z. Sun, J. Magn. Magn. Mater. **202**, 157 (1999).

[17]J. Z. Sun, Phys. Rev. B **62**, 570 (2000).

[18]S. S. P. Parkin, M. Hayashi, and L. Thomas, Science **320**, 190 (2008).

[19]R. Bläsing, A. A. Khan, P. C. Filippou, F. Hameed, J. Castrillon, and S. S. P. Parkin, Proc. IEEE **108**, 1303 (2020).

[20]K.-S. Lee, S.-W. Lee, B.-C. Min, and K.-J. Lee, Appl. Phys. Lett. **102**, 112410 (2013).

[21]K.-S. Lee, S.-W. Lee, B.-C. Min, and K.-J. Lee, Appl. Phys. Lett. **104**, 072413 (2014).

[22]W. Kang, Y. Huang, X. Zhang, Y. Zhou, and W. Zhao, Proc. IEEE **104**, 2040 (2016).

[23]G. Finocchio, F. Büttner, R. Tomasello, M. Carpentieri, and M. Kläui, J. Phys. D: Appl. Phys. **49**, 423001 (2016).

[24]K. Everschor-Sitte, J. Masell, R. M. Reeve, and M. Kläui, J. Appl. Phys. **124**, 240901 (2018).

[25]S. Li, W. Kang, X. Zhang, T. Nie, Y. Zhou, K. L. Wang, and W. Zhao, Mater. Horiz. **8**, 854 (2021).

[26]S. Mühlbauer, B. Binz, F. Jonietz, C. Pfleiderer, A. Rosch, A. Neubauer, R. Georgii, and P. Böni, Science **323**, 915 (2009).

[27]A. Neubauer, C. Pfleiderer, B. Binz, A. Rosch, R. Ritz, P. G. Niklowitz, and P. Böni, Phys. Rev. Lett. **102**, 186602 (2009).

[28]T. Adams, S. Mühlbauer, C. Pfleiderer, F. Jonietz, A. Bauer, A. Neubauer, R. Georgii, P. Böni, U. Keiderling, K. Everschor, M. Garst, and A. Rosch, Phys. Rev. Lett. **107**, 217206 (2011).

[29]S. Mühlbauer, J. Kindervater, T. Adams, A. Bauer, U. Keiderling, and C. Pfleiderer, New J. Phys. **18**, 075017 (2016).

[30]M. Lee, W. Kang, Y. Onose, Y. Tokura, and N. P. Ong, Phys. Rev. Lett. **102**, 186601 (2009).

[31]R. Ritz, M. Halder, C. Franz, A. Bauer, M. Wagner, R. Bamler, A. Rosch, and C. Pfleiderer, Phys. Rev. B **87**, 134424 (2013).

[32]A. Chacon, A. Bauer, T. Adams, F. Rucker, G. Brandl, R. Georgii, M. Garst, and C. Pfleiderer, Phys. Rev. Lett. **115**, 267202 (2015).

[33]S.-G. Je, H.-S. Han, S. K. Kim, S. A. Montoya, W. Chao, I.-S. Hong, E. E. Fullerton, K.-S. Lee, K.-J. Lee, M.-Y. Im, and J.-I. Hong, ACS Nano **14**, 3251 (2020).

[34]H. Goldstein, C. P. Poole, and J. L. Safko, *Classical Mechanics*, 3rd ed. (Addison-Wesley, 2001).

[35]K. Litzius, F. Büttner, A. Wittmann, W. Zhou, C. T. Ma, J. Gräfe, N. A. Träger, S. Finizio, Y. Quessab, D. Suzuki, L. Caretta, M. Huang, S. Sheffels, S. Huang, H. T. Nembach, G. A. Riley, J. M. Shaw, M. Valvidares, P. Gargiani, G. Schütz, A. D. Kent, S. J. Poon, and G. S. D. Beach, "Universal high-speed dynamics of distorted bubble skyrmions in an uncompensated amorphous ferrimagnet" (to be published) (2020).

[36]S. Rohart and A. Thiaville, Phys. Rev. B **88**, 184422 (2013).

[37]A. N. Bogdanov and U. K. Rößler, Phys. Rev. Lett. **87**, 037203 (2001).

[38]F. Büttner, I. Lemesh, and G. S. D. Beach, Sci. Rep. **8**, 4464 (2018).

[39]X. S. Wang, H. Y. Yuan, and X. R. Wang, Commun. Phys. **1**, 31 (2018).

[40]Y. Xie, J. Ma, H. Vakilitaleghani, Y. Tan, and A. W. Ghosh, IEEE Trans. Magn. **56**, 1 (2020).

[41]A. A. Thiele, Phys. Rev. Lett. **30**, 230 (1973).

[42]A. Hrabec, J. Sampaio, M. Belmeguenai, I. Gross, R. Weil, S. M. Chérif, A. Stashkevich, V. Jacques, A. Thiaville, and S. Rohart, Nat. Commun. **8**, 15765 (2017).

[43]R. Tomasello, E. Martinez, R. Zivieri, L. Torres, M. Carpentieri, and G. Finocchio, Sci. Rep. **4**, 6784 (2014).

[44]C. Reichhardt and C. J. Olson Reichhardt, New J. Phys. **18**, 095005 (2016).

[45]K. Litzius, I. Lemesh, B. Krüger, P. Bassirian, L. Caretta, K. Richter, F. Büttner, K. Sato, O. A. Tretiakov, J. Förster, R. M. Reeve, M. Weigand, I. Bykova, H. Stoll, G. Schütz, G. S. D. Beach, and M. Kläui, Nat. Phys. **13**, 170 (2017).

[46]K. Litzius, J. Leliaert, P. Bassirian, D. Rodrigues, S. Kromin, I. Lemesh, J. Zazvorka, K.-J. Lee, J. Mulkers, N. Kerber, D. Heinze, N. Keil, R. M. Reeve, M. Weigand, B. Van Waeyenberge, G. Schütz, K. Everschor-Sitte, G. S. D. Beach, and M. Kläui, Nat. Electron. **3**, 30 (2020).

[47]W. Jiang, X. Zhang, G. Yu, W. Zhang, X. Wang, M. Benjamin Jungfleisch, J. E. Pearson, X. Cheng, O. Heinonen, K. L. Wang, Y. Zhou, A. Hoffmann, and S. G. E. te Velthuis, Nat. Phys. **13**, 162 (2017).

[48]R. Juge, S.-G. Je, D. d. S. Chaves, L. D. Buda-Prejbeanu, J. Peña Garcia, J. Nath, I. M. Miron, K. G. Rana, L. Aballe, M. Foerster, F. Genuzio, T. O. Mentes, A. Locatelli, F. Maccherozzi, S. S. Dhesi, M. Belmeguenai, Y. Roussigné, S. Auffret, S. Pizzini, G. Gaudin, J. Vogel, and O. Boulle, Phys. Rev. Appl. **12**, 044007 (2019).

[49]F. D. M. Haldane, Phys. Rev. Lett. **50**, 1153 (1983).

[50]S. K. Kim, Y. Tserkovnyak, and O. Tchernyshyov, Phys. Rev. B **90**, 104406 (2014).

[51]N. Romming, C. Hanneken, M. Menzel, J. E. Bickel, B. Wolter, K. von Bergmann, A. Kubetzka, and R. Wiesendanger, Science **341**, 636 (2013).

[52]J. Ma, V. I. Hegde, K. Munira, Y. Xie, S. Keshavarz, D. T. Mildebrath, C. Wolverton, A. W. Ghosh, and W. H. Butler, Phys. Rev. B **95**, 024411 (2017).

[53]S. Woo, K. Litzius, B. Krüger, M.-Y. Im, L. Caretta, K. Richter, M. Mann, A. Krone, R. M. Reeve, M. Weigand, P. Agrawal, I. Lemesh, M.-A. Mawass, P. Fischer, M. Kläui, and G. S. D. Beach, Nat. Mater. **15**, 501 (2016).

[54]A. Soumyanarayanan, M. Raju, A. L. Gonzalez Oyarce, A. K. C. Tan, M.-Y. Im, A. Petrović, P. Ho, K. H. Khoo, M. Tran, C. K. Gan, F. Ernult, and C. Panagopoulos, Nat. Mater. **16**, 898 (2017).

[55]V. G. Harris, K. D. Aylesworth, B. N. Das, W. T. Elam, and N. C. Koon, Phys. Rev. Lett. **69**, 1939 (1992).

[56]L. Caretta, M. Mann, F. Büttner, K. Ueda, B. Pfau, C. M. Günther, P. Hessing, A. Churikova, C. Klose, M. Schneider, D. Engel, C. Marcus, D. Bono, K. Bagschik, S. Eisebitt, and G. S. D. Beach, Nat. Nanotechnol. **13**, 1154 (2018).

[57]C. T. Ma, Y. Xie, H. Sheng, A. W. Ghosh, and S. J. Poon, Sci. Rep. **9**, 9964 (2019).

[58]Y. Quessab, J.-W. Xu, C. T. Ma, W. Zhou, G. A. Riley, J. M. Shaw, H. T. Nembach, S. J. Poon, and A. D. Kent, Sci. Rep. **10**, 7447 (2020).

[59]G. Schütz, E. Goering, and H. Stoll, Int. J. Mater. Res. **102**, 773 (2011).

[60]Z. Wang, M. Guo, H.-A. Zhou, L. Zhao, T. Xu, R. Tomasello, H. Bai, Y. Dong, S.-G. Je, W. Chao, H.-S. Han, S. Lee, K.-S. Lee, Y. Yao, W. Han, C. Song, H. Wu, M. Carpentieri, G. Finocchio, M.-Y. Im, S.-Z. Lin, and W. Jiang, Nat. Electron. **3**, 672 (2020).

[61]K. Ueda, A. J. Tan, and G. S. D. Beach, AIP Adv. **8**, 125204 (2018).

[62]F. Nabki, T. A. Dusatko, S. Vengallatore, and M. N. El-Gamal, J. Microelectromech. Syst. **20**, 720 (2011).

[63]S. Isogami, K. Masuda, and Y. Miura, Phys. Rev. Mater. **4**, 014406 (2020).

[64]W. Zhou, C. T. Ma, T. Q. Hartnett, P. V. Balachandran, and S. J. Poon, AIP Adv. **11**, 015334 (2021).

[65]W. J. Takei, R. R. Heikes, and G. Shirane, Phys. Rev. **125**, 1893 (1962).

[66]P. Giannozzi, S. Baroni, N. Bonini, M. Calandra, R. Car, C. Cavazzoni, D. Ceresoli, G. L. Chiarotti, M. Cococcioni, I. Dabo, A. Dal Corso, S. de Gironcoli, S. Fabris, G. Fratesi, R. Gebauer, U. Gerstmann, C. Gougoussis, A. Kokalj, M. Lazzeri, L. Martin-Samos, N. Marzari, F. Mauri, R. Mazzarello, S. Paolini, A. Pasquarello, L. Paulatto, C. Sbraccia, S. Scandolo, G. Sclauzero, A. P. Seitsonen, A. Smogunov, P. Umari, and R. M. Wentzcovitch, J. Phys.: Condens. Matter **21**, 395502 (2009).

[67]R. F. L. Evans, W. J. Fan, P. Chureemart, T. A. Ostler, M. O. A. Ellis, and R. W. Chantrell, J. Phys.: Condens. Matter **26**, 103202 (2014).

[68]J. Kübler, A. R. William, and C. B. Sommers, Phys. Rev. B **28**, 1745 (1983).

[69]S. Woo, K. M. Song, X. Zhang, Y. Zhou, M. Ezawa, X. Liu, S. Finizio, J. Raabe, N. J. Lee, S.-I. Kim, S.-Y. Park, Y. Kim, J.-Y. Kim, D. Lee, O. Lee, J. W. Choi, B.-C. Min, H. C. Koo, and J. Chang, Nat. Commun. **9**, 959 (2018).

[70]E. Şaşioğlu, L. M. Sandratskii, and P. Bruno, J. Phys.: Condens. Matter **17**, 995 (2005).

[71]T. Dohi, S. DuttaGupta, S. Fukami, and H. Ohno, Nat. Commun. **10**, 5153 (2019).

[72]W. Legrand, D. Maccariello, F. Ajejas, S. Collin, A. Vecchiola, K. Bouzehouane, N. Reyren, V. Cros, and A. Fert, Nat. Mater. **19**, 34 (2020).

[73]H. Yang, A. Thiaville, S. Rohart, A. Fert, and M. Chshiev, Phys. Rev. Lett. **115**, 267210 (2015).

[74]A. Belabbes, G. Bihlmayer, F. Bechstedt, S. Blügel, and A. Manchon, Phys. Rev. Lett. **117**, 247202 (2016).

[75]P. Jadaun, L. F. Register, and S. K. Banerjee, npj Comput. Mater. **6**, 1 (2020).

[76]O. Boulle, J. Vogel, H. Yang, S. Pizzini, D. de Souza Chaves, A. Locatelli, T. O. Menteş, A. Sala, L. D. Buda-Prejbeanu, O. Klein, M. Belmeguenai, Y. Roussigné, A. Stashkevich, S. M. Chérif, L. Aballe, M. Foerster, M. Chshiev, S. Auffret, I. M. Miron, and G. Gaudin, Nat. Nanotechnol. **11**, 449 (2016).

[77]M. Arora, J. M. Shaw, and H. T. Nembach, Phys. Rev. B **101**, 054421 (2020).

[78]C. Moreau-Luchaire, C. Moutafis, N. Reyren, J. Sampaio, C. A. F. Vaz, N. Van Horne, K. Bouzehouane, K. Garcia, C. Deranlot, P. Warnicke, P. Wohlhüter, J. M. George, M. Weigand, J. Raabe, V. Cros, and A. Fert, Nat. Nanotechnol. **11**, 444 (2016).

[79]W. Legrand, D. Maccariello, N. Reyren, K. Garcia, C. Moutafis, C. Moreau-Luchaire, S. Collin, K. Bouzehouane, V. Cros, and A. Fert, Nano Lett. **17**, 2703 (2017).

[80]L. Zhu, K. Sobotkiewich, X. Ma, X. Li, D. C. Ralph, and R. A. Buhrman, Adv. Funct. Mater. **29**, 1805822 (2019).

[81]M. G. Morshed, K. H. Khoo, Y. Quessab, J.-W. Xu, R. Laskowski, P. V. Balachandran, A. D. Kent, and A. W. Ghosh, Phys. Rev. B **103**, 174414 (2021).

[82]T. Srivastava, M. Schott, R. Juge, V. Křižáková, M. Belmeguenai, Y. Roussigné, A. Bernand-Mantel, L. Ranno, S. Pizzini, S.-M. Chérif, A. Stashkevich, S. Auffret, O. Boulle, G. Gaudin, M. Chshiev, C. Baraduc, and H. Béa, Nano Lett. **18**, 4871 (2018).

[83]L. Herrera Diez, Y. T. Liu, D. A. Gilbert, M. Belmeguenai, J. Vogel, S. Pizzini, E. Martinez, A. Lamperti, J. B. Mohammedi, A. Laborieux, Y. Roussigné, A. J. Grutter, E. Arenholtz, P. Quarterman, B. Maranville, S. Ono, M. S. E. Hadri, R. Tolley, E. E. Fullerton, L. Sanchez-Tejerina, A. Stashkevich, S. M. Chérif, A. D. Kent, D. Querlioz, J. Langer, B. Ocker, and D. Ravelosona, Phys. Rev. Appl. **12**, 034005 (2019).

[84]L. H. Diez, M. Voto, A. Casiraghi, M. Belmeguenai, Y. Roussigné, G. Durin, A. Lamperti, R. Mantovan, V. Sluka, V. Jeudy, Y. T. Liu, A. Stashkevich, S. M. Chérif, J. Langer, B. Ocker, L. Lopez-Diaz, and D. Ravelosona, Phys. Rev. B **99**, 054431 (2019).

[85]G. Chen, A. Mascaraque, A. T. N'Diaye, and A. K. Schmid, Appl. Phys. Lett. **106**, 242404 (2015).

[86]F. Zheng, H. Li, S. Wang, D. Song, C. Jin, W. Wei, A. Kovács, J. Zang, M. Tian, Y. Zhang, H. Du, and R. E. Dunin-Borkowski, Phys. Rev. Lett. **119**, 197205 (2017).

[87]J. C. Gallagher, K. Y. Meng, J. T. Brangham, H. L. Wang, B. D. Esser, D. W. McComb, and F. Y. Yang, Phys. Rev. Lett. **118**, 027201 (2017).

[88]J. Müller, New J. Phys. **19**, 025002 (2017).

[89]S. Finizio, K. Zeissler, S. Wintz, S. Mayr, T. Weßels, A. J. Huxtable, G. Burnell, C. H. Marrows, and J. Raabe, Nano Lett. **19**, 7246 (2019).

[90]S.-G. Je, D. Thian, X. Chen, L. Huang, D.-H. Jung, W. Chao, K.-S. Lee, J.-I. Hong, A. Soumyanarayanan, and M.-Y. Im, Nano Lett. **21**, 1253 (2021).

[91]I. Lemesh, K. Litzius, M. Böttcher, P. Bassirian, N. Kerber, D. Heinze, J. Zázvorka, F. Büttner, L. Caretta, M. Mann, M. Weigand, S. Finizio, J. Raabe, M.-Y. Im, H. Stoll, G. Schütz, B. Dupé, M. Kläui, and G. S. D. Beach, Adv. Mater. **30**, 1805461 (2018).

[92]S. Woo, K. M. Song, X. Zhang, M. Ezawa, Y. Zhou, X. Liu, M. Weigand, S. Finizio, J. Raabe, M.-C. Park, K.-Y. Lee, J. W. Choi, B.-C. Min, H. C. Koo, and J. Chang, Nat. Electron. **1**, 288 (2018).

[93]K. M. Song, J.-S. Jeong, B. Pan, X. Zhang, J. Xia, S. Cha, T.-E. Park, K. Kim, S. Finizio, J. Raabe, J. Chang, Y. Zhou, W. Zhao, W. Kang, H. Ju, and S. Woo, Nat. Electron. **3**, 148 (2020).

[94]S. Woo, K. M. Song, H.-S. Han, M.-S. Jung, M.-Y. Im, K.-S. Lee, K. S. Song, P. Fischer, J.-I. Hong, J. W. Choi, B.-C. Min, H. C. Koo, and J. Chang, Nat. Commun. **8**, 015573 (2017).

[95]F. Büttner, I. Lemesh, M. Schneider, B. Pfau, C. M. Günther, P. Hessing, J. Geilhufe, L. Caretta, D. Engel, B. Krüger, J. Viefhaus, S. Eisebitt, and G. S. D. Beach, Nat. Nanotechnol. **12**, 1040 (2017).

[96]W. Koshibae and N. Nagaosa, Nat. Commun. **5**, 5148 (2014).

[97]T. Yokouchi, S. Sugimoto, B. Rana, S. Seki, N. Ogawa, S. Kasai, and Y. Otani, Nat. Nanotechnol. **15**, 361 (2020).

[98]S.-G. Je, P. Vallobra, T. Srivastava, J.-C. Rojas-Sánchez, T. H. Pham, M. Hehn, G. Malinowski, C. Baraduc, S. Auffret, G. Gaudin, S. Mangin, H. Béa, and O. Boulle, Nano Lett. **18**, 7362 (2018).

[99]M. Finazzi, M. Savoini, A. R. Khorsand, A. Tsukamoto, A. Itoh, L. Duò, A. Kirilyuk, T. Rasing, and M. Ezawa, Phys. Rev. Lett. **110**, 177205 (2013).

[100]F. Büttner, M. A. Mawass, J. Bauer, E. Rosenberg, L. Caretta, C. O. Avci, J. Gräfe, S. Finizio, C. A. F. Vaz, N. Novakovic, M. Weigand, K. Litzius, J. Förster, N. Träger, F. Groß, D. Suzuki, M. Huang, J. Bartell, F. Kronast, J. Raabe, G. Schütz, C. A. Ross, and G. S. D. Beach, Phys. Rev. Mater. **4**, 011401 (2020).

[101]S. Ding, A. Ross, R. Lebrun, S. Becker, K. Lee, I. Boventer, S. Das, Y. Kurokawa, S. Gupta, J. Yang, G. Jakob, and M. Kläui, Phys. Rev. B **100**, 100406 (2019).

[102]Y. Nakatani, M. Hayashi, S. Kanai, S. Fukami, and H. Ohno, Appl. Phys. Lett. **108**, 152403 (2016).

[103]M. Schott, A. Bernand-Mantel, L. Ranno, S. Pizzini, J. Vogel, H. Béa, C. Baraduc, S. Auffret, G. Gaudin, and D. Givord, Nano Lett. **17**, 3006 (2017).

[104]D. Bhattacharya, S. A. Razavi, H. Wu, B. Dai, K. L. Wang, and J. Atulasimha, Nat. Electron. **3**, 539 (2020).

[105]S. M. Wu, S. A. Cybart, P. Yu, M. D. Rossell, J. X. Zhang, R. Ramesh, and R. C. Dynes, Nat. Mater. **9**, 756 (2010).

[106]S. M. Wu, S. A. Cybart, D. Yi, J. M. Parker, R. Ramesh, and R. C. Dynes, Phys. Rev. Lett. **110**, 067202 (2013).

[107]H.-B. Li, N. Lu, Q. Zhang, Y. Wang, D. Feng, T. Chen, S. Yang, Z. Duan, Z. Li, Y. Shi, W. Wang, W.-H. Wang, K. Jin, H. Liu, J. Ma, L. Gu, C. Nan, and P. Yu, Nat. Commun. **8**, 2156 (2017).

[108]Q. Yang, Z. Zhou, N. X. Sun, and M. Liu, Phys. Lett. A **381**, 1213 (2017).

[109]Y. Guang, I. Bykova, Y. Liu, G. Yu, E. Goering, M. Weigand, J. Gräfe, S. K. Kim, J. Zhang, H. Zhang, Z. Yan, C. Wan, J. Feng, X. Wang, C. Guo, H. Wei, Y. Peng, Y. Tserkovnyak, X. Han, and G. Schütz, Nat. Commun. **11**, 949 (2020).

[110]S. Zhang, A. K. Petford-Long, and C. Phatak, Sci. Rep. **6**, 031248 (2016).

[111]G. Henkelman, B. P. Uberuaga, and H. Jónsson, J. Chem. Phys. **113**, 9901 (2000).

[112]P. F. Bessarab, V. M. Uzdin, and H. Jónsson, Phys. Rev. B **85**, 184409 (2012).

[113]P. F. Bessarab, V. M. Uzdin, and H. Jónsson, Comput. Phys. Commun. **196**, 335 (2015).

[114]J. Wild, T. N. G. Meier, S. Pöllath, M. Kronseder, A. Bauer, A. Chacon, M. Halder, M. Schowalter, A. Rosenauer, J. Zweck, J. Müller, A. Rosch, C. Pfleiderer, and C. H. Back, Sci. Adv. **3**, e1701704 (2017).

[115]F. Muckel, S. von Malottki, C. Holl, B. Pestka, M. Pratzer, P. F. Bessarab, S. Heinze, and M. Morgenstern, Nat. Phys. **17**, 395 (2021).

[116]M. Hoffmann, G. P. Müller, and S. Blügel, Phys. Rev. Lett. **124**, 247201 (2020).

[117]R. E. Troncoso and Á. S. Núñez, Ann. Phys. **351**, 850 (2014).

[118]L. Zhao, Z. Wang, X. Zhang, X. Liang, J. Xia, K. Wu, H.-A. Zhou, Y. Dong, G. Yu, K. L. Wang, X. Liu, Y. Zhou, and W. Jiang, Phys. Rev. Lett. **125**, 027206 (2020).

[119]G. Beach, private communication (24 July 2020).

[120]P. F. Bessarab, G. P. Müller, I. S. Lobanov, F. N. Rybakov, N. S. Kiselev, H. Jónsson, V. M. Uzdin, S. Blügel, L. Bergqvist, and A. Delin, Sci. Rep. **8**, 3433 (2018).

[121]D. Suess, C. Vogler, F. Bruckner, P. Heistracher, F. Slanovc, and C. Abert, Sci. Rep. **9**, 4827 (2019).

[122]W. E. W. Ren and E. Vanden-Eijnden, Phys. Rev. B **66**, 052301 (2002).

[123]H. Vakili, M. N. Sakib, S. Ganguly, M. Stan, M. W. Daniels, A. Madhavan, M. D. Stiles, and A. W. Ghosh, IEEE J. Exploratory Solid-State Comput. Devices Circuits **6**, 107 (2020).

[124]A. Madhavan, T. Sherwood, and D. Strukov, in *2014 ACM/IEEE 41st International Symposium on Computer Architecture (ISCA)* (IEEE, 2014), Vol. 517. ISSN: 1063-6897.

[125]A. Madhavan, T. Sherwood, and D. Strukov, in *2017 IEEE Custom Integrated Circuits Conference (CICC)* (IEEE, 2017), Vol. 1.

[126]G. Tzimpragos, A. Madhavan, D. Vasudevan, D. Strukov, and T. Sherwood, in *Proceedings of the Twenty-Forth International Conference on Architectural Support for Programming Languages and Operating Systems ASPLOS '19* (ACM, 2019).

[127]A. Madhavan, M. Daniels, and M. Stiles, arXiv:2009.14243 (2020).

[128]I. Kuon, R. Tessier, and J. Rose, *FPGA Architecture: Survey and Challenges* (Now Publishers Inc., 2008).

[129]X. Zhang, M. Ezawa, and Y. Zhou, Sci. Rep. **5**, 9400 (2015).

[130]S. Luo, M. Song, X. Li, Y. Zhang, J. Hong, X. Yang, X. Zou, N. Xu, and L. You, Nano Lett. **18**, 1180 (2018).

[131]Z. Zhang, Y. Zhu, Y. Zhang, K. Zhang, J. Nan, Z. Zheng, Y. Zhang, and W. Zhao, IEEE Electron Device Lett. **40**, 1984 (2019).

[132]H. Vakili, Y. Xie, and A. W. Ghosh, Phys. Rev. B **102**, 174420 (2020).

[133]M. N. Sakib, H. Vakili, S. Ganguly, S. Mosanu, A. W. Ghosh, and M. Stan, Proc. SPIE **11470**, 114703D (2020).

[134]H. Zhang, D. Zhu, W. Kang, Y. Zhang, and W. Zhao, Phys. Rev. Appl. **13**, 054049 (2020).

[135]N. R. Shanbhag, R. A. Abdallah, R. Kumar, and D. L. Jones, in *Proceedings of the 47th Design Automation Conference* (ACM, 2010), Vol. 859.

[136]S. Toral, J. Quero, and L. Franquelo, in *2000 IEEE International Symposium on Circuits and Systems (ISCAS)* (IEEE, 2000), Vol. 1, p. 599

[137]W. Qian and M. D. Riedel, in *2008 45th ACM/IEEE Design Automation Conference* (ACM, 2008), Vol. 648.

[138]X. Li, W. Qian, M. D. Riedel, K. Bazargan, and D. J. Lilja, in *Proceedings of the 19th ACM Great Lakes symposium on VLSI* (ACM, 2009), Vol. 315.

[139]W. Qian, X. Li, M. D. Riedel, K. Bazargan, and D. J. Lilja, IEEE Trans. Comput. **60**, 93 (2011).

[140]P. Mars and H. McLean, Electron. Lett. **12**, 457 (1976).

[141]D. Zhang and H. Li, IEEE Trans. Ind. Electron. **55**, 551 (2008).

[142]D. Pinna, F. A. Araujo, J.-V. Kim, V. Cros, D. Querlioz, P. Bessiere, J. Droulez, and J. Grollier, Phys. Rev. Appl. **9**, 064018 (2018).

[143]J. Zázvorka, F. Jakobs, D. Heinze, N. Keil, S. Kromin, S. Jaiswal, K. Litzius, G. Jakob, P. Virnau, D. Pinna, K. Everschor-Sitte, L. Rózsa, A. Donges, U. Nowak, and M. Kläui, Nat. Nanotechnol. **14**, 658 (2019).

[144]M. W. Daniels, A. Madhavan, P. Talatchian, A. Mizrahi, and M. D. Stiles, Phys. Rev. Appl. **13**, 034016 (2020).

[145]Y. Huang, W. Kang, X. Zhang, Y. Zhou, and W. Zhao, Nanotechnology **28**, 08LT02 (2017).

[146]Z. He and D. Fan, arXiv:1705.02995 (2017).

[147]Z. He and D. Fan, in *Proc. IEEE Design Autom. Test Eur. Conf. Exhibit.* (IEEE, 2017), Vol. 350.

[148]S. Ganguly, K. Y. Camsari, and A. W. Ghosh, IEEE Access **9**, 092640 (2021).

[149]G. Bourianoff, D. Pinna, M. Sitte, and K. Everschor-Sitte, AIP Adv. **8**, 055602 (2018).

[150]D. Prychynenko, M. Sitte, K. Litzius, B. Krüger, G. Bourianoff, M. Kläui, J. Sinova, and K. Everschor-Sitte, Phys. Rev. Appl. **9**, 014034 (2018).

[151]S. Zhang, J. Wang, Q. Zheng, Q. Zhu, X. Liu, S. Chen, C. Jin, Q. Liu, C. Jia, and D. Xue, New J. Phys. **17**, 023061 (2015).

[152]F. Garcia-Sanchez, J. Sampaio, N. Reyren, V. Cros, and J.-V. Kim, New J. Phys. **18**, 075011 (2016).

[153]M. Chauwin, X. Hu, F. Garcia-Sanchez, N. Betrabet, A. Paler, C. Moutafis, and J. S. Friedman, Phys. Rev. Appl. **12**, 064053 (2019).

[154]A. S. Núñez, R. A. Duine, P. Haney, and A. H. MacDonald, Phys. Rev. B **73**, 214426 (2006).

[155]V. Baltz, A. Manchon, M. Tsoi, T. Moriyama, T. Ono, and Y. Tserkovnyak, Rev. Mod. Phys. **90**, 015005 (2018).

[156]Y. Su, J. Zhang, J.-T. Lü, J. Hong, and L. You, Phys. Rev. Appl. **12**, 044036 (2019).

[157]B. Dieny, J. Magn. Magn. Mater. **136**, 335 (1994).

[158]K. Inomata, T. Nozaki, N. Tezuka, and S. Sugimoto, Appl. Phys. Lett. **81**, 310 (2002).

[159]W. Zhao, C. Chappert, V. Javerliac, and J.-P. Noziere, IEEE Trans. Magn. **45**, 3784 (2009).

[160]D. Maccariello, W. Legrand, N. Reyren, K. Garcia, K. Bouzehouane, S. Collin, V. Cros, and A. Fert, Nat. Nanotech. **13**, 233 (2018).

[161]X. Zhang, Y. Zhou, K. M. Song, T.-E. Park, J. Xia, M. Ezawa, X. Liu, W. Zhao, G. Zhao, and S. Woo, J. Phys.: Condens. Matter **32**, 143001 (2020).

[162]B. Göbel, I. Mertig, and O. A. Tretiakov, Phys. Rep. **895**, 1–28 (2020).

[163]A. Salimath, F. Zhuo, R. Tomasello, G. Finocchio, and A. Manchon, Phys. Rev. B **101**, 024429 (2020).